Networks and Heterogeneous Media

https://www.aimspress.com/journal/nhm

NHM, 21(2): 564–593.
DOI: 10.3934/nhm.2026026
Received: 16 September 2025
Revised: 18 March 2026
Accepted: 24 March 2026
Published: 13 April 2026

Research article

MHD flow and heat transfer of fractional nanofluids in a porous medium with ramped wall temperature and heat injection/consumption

Huafang Li[1], Zhi Mao[2,3,*], Aiguo Xiao[3], Libo Feng[4], Leilei Wei[5] and Fawang Liu[6]

[1] School of Mathematics and Statistics, Jishou University, Jishou 416000, China

[2] School of Data Science, Tongren University, Tongren 554300, China

[3] Key Laboratory of Intelligent Computing and Information Processing, Ministry of Education, Xiangtan University, Xiangtan 411105, China

[4] School of Mathematical Sciences, Queensland University of Technology, GPO Box 2434, Brisbane, Qld. 4001, Australia

[5] School of Mathematics and Statistics, Henan University of Technology, Zhengzhou 450001, China

[6] School of Mathematics and Statistics, Fuzhou University, Fuzhou 350108, China

* **Correspondence:** Email: yjsymz@gztrc.edu.cn; Tel: +8608568121276; Fax: +8608568121809.

Abstract: This study focused on the unsteady magnetohydrodynamic (MHD) flow and heat transfer of fractional viscoelastic nanofluids over an infinite vertical plate within a porous medium. Both ramped and isothermal wall temperature conditions were considered, along with the effects of heat injection and consumption. The momentum equation was formulated based on a dual-parameter fractional Maxwell constitutive relation, while the energy equation incorporated a fractional dual-phase-lag (DPL) model. The resulting fractional integrodifferential governing equations were solved numerically using a finite difference method combined with the L1 algorithm and the weighted-shifted Grünwald difference scheme. The accuracy of the proposed numerical scheme was verified through manufactured solutions. Numerical results show that increasing porous medium permeability enhances fluid flow, whereas a stronger magnetic field suppresses it. The effects of the phase-lag parameters on the thermal boundary layer differ under ramped and isothermal wall temperature conditions: the phase lag of the temperature gradient leads to a monotonic thickening in the former but a nonmonotonic variation in the latter, whereas the phase lag of the heat flux exhibits an opposite trend. This study provides valuable insights into the application of fractional integrodifferential models for the design and optimization of thermal systems involving nanofluids.

Keywords: nanofluids; MHD flow; heat transfer; dual-parameter fractional Maxwell model; fractional dual-phase-lag model

1. Introduction

A nanofluid is a homogeneous mixture of a base fluid and nanoparticles with characteristic sizes smaller than 100 nm, first introduced by Choi and Eastman [1]. Common base fluids include water, ethylene glycol, and various oils [2], while the suspended nanoparticles are typically metals: metal oxides, metal carbides, or carbon-based materials. The thermophysical properties of nanofluids depend on several factors, including the type, shape, and size of nanoparticles, their stability in the base fluid, and the properties of the base fluid itself [3]. For example, Eastman et al. [4] showed that the addition of copper nanoparticles to ethylene glycol can significantly enhance thermal conductivity. Owing to their superior heat transfer performance, nanofluids have found widespread applications in electronic cooling, oil recovery, refrigeration, solar energy systems, and desalination [5]. Consequently, the transport behavior of nanofluids has been extensively studied, leading to the development of various models for describing their flow and heat transfer characteristics. These studies have addressed different thermophysical aspects, such as thermal conductivity [4], density [6], and viscosity [7]. However, classical Newtonian constitutive relations are often inadequate for describing complex transport behavior in nanofluids, especially when memory effects, viscoelasticity, and anomalous transport processes become important. To overcome these limitations, fractional calculus has been incorporated into generalized constitutive models, providing a more flexible framework for characterizing the rheological behavior of complex fluids. In recent years, fractional-order models have been increasingly applied to viscoelastic nanofluid dynamics. Zhao et al. [8] established boundary-layer equations for viscoelastic nanofluids based on a fractional Maxwell model, while Shen et al. [9] extended the Buongiorno model by employing a fractional Cattaneo constitutive relation to analyze the heat and mass transfer behavior of Sisko nanofluids. Liu et al. [10] investigated laminar boundary-layer flow over a moving plate using a distributed-order time-fractional Maxwell constitutive relation, Feng et al. [11] proposed a generalized Kelvin–Voigt constitutive framework for nanofluid thermal boundary layers, and Mao et al. [12] derived fractional integrodifferential governing equations based on a dual-parameter fractional Maxwell constitutive relation to study the natural convection flow of nanofluids. These studies indicate that fractional constitutive modeling has become an important direction in the current development of nanofluid transport theory. For further related work on fractional constitutive models in viscoelastic fluids, readers are referred to refs. [13–15].

Magnetohydrodynamic (MHD) flow and radiative heat transfer also play important roles in many natural and engineering processes, such as volcanic eruptions, auroras, solar flares [16], heat exchangers, geothermal extraction equipment, and aerospace propulsion systems [17]. In electrically conducting nanofluids, the application of a magnetic field generates electromagnetic forces that can significantly modify the velocity field, thermal boundary layer development, and overall transport behavior. For this reason, the study of MHD flow and heat transfer in nanofluids and viscoelastic fluids has attracted considerable attention. Chamkha and Aly [18] examined natural convection in nanofluids under the combined effects of the magnetic field, nanoparticles, and heat generation. Anwar et al. [19] investigated MHD convective flow of an Oldroyd-B fluid in a porous channel with nonlinear thermal radiation. Dharmaiah et al. [20] studied nonlinear radiative MHD effects on micropolar nanofluid flow over a stretching surface, while Bejawada and Nandeppanavar [21] analyzed MHD heat transfer in micropolar fluid flow along a vertical porous plate by considering

micro-rotation, thermal radiation, and magnetic effects. Saleem et al. [22] further employed intelligent computing techniques to simulate chemically reactive and radiative magnetized Casson nanofluids over a nonlinear stretching sheet. More recently, Sheng et al. [23] developed a new MHD model to investigate the coupled flow, heat, and mass transfer of a fractional Oldroyd-B fluid along a moving vertical plate. These contributions show that the combined effects of the magnetic field, radiation, and porous structures have become an important part of the current state-of-the-art works in complex nanofluid transport research. Additional studies in this direction can be found in refs. [24, 25].

Another important aspect in transient heat transfer is the thermal boundary condition at the wall. In many practical heating processes, the wall temperature does not rise instantaneously to a prescribed value but instead increases gradually with time. Therefore, ramped wall temperature conditions often provide a more realistic description than idealized isothermal heating. Such conditions are relevant to thermal startup and controlled heating processes [26], and have consequently attracted increasing research interest. Ahmed and Dutta [27] first introduced ramped wall velocity and temperature conditions to study transient flow and mass transfer over an oscillating plate. Chandran et al. [28] subsequently examined the influence of ramped wall temperature on convective flow of viscous fluids, and Seth et al. [29] extended this analysis by incorporating porous medium effects. More recently, Rao and Deka [30] investigated the heat transfer characteristics of a Casson hybrid nanofluid over a vertically stretched plate under magnetic influence, showing that ramped wall temperature and velocity conditions can significantly modify flow behavior and thermal transport performance. These studies demonstrate that the wall heating mode is a key factor in transient boundary-layer development and should be carefully considered in nanofluid heat transfer analysis. Further related studies on ramped wall temperature conditions are available in refs. [31–33].

Although previous studies have examined MHD effects, porous medium flow, fractional viscoelastic behavior, and ramped wall heating from different perspectives, their combined effects on unsteady nanofluid flow and heat transfer have not been sufficiently explored within a unified fractional framework. Motivated by this physical consideration and recent developments in fractional nanofluid modeling, the objective of the present study is to examine the unsteady MHD flow and heat transfer of fractional viscoelastic nanofluids past an infinite vertical plate in a porous medium under ramped and isothermal wall temperature conditions, while also accounting for heat injection/consumption. The main contributions of this paper include:

• A fractional integrodifferential model is developed for the unsteady MHD flow and heat transfer of viscoelastic nanofluids in a porous medium. In this model, the momentum equation is derived from a dual-parameter fractional Maxwell constitutive relation, while the energy equation is formulated through a fractional dual-phase-lag heat conduction law. The model also incorporates ramped and isothermal wall temperature conditions together with heat injection/consumption effects.

• A finite difference framework is developed for the coupled fractional governing equations. Its numerical accuracy is verified through manufactured solutions, while its reliability is further supported by comparisons with several classical nanofluid models. The comparison results indicate that the constructed fractional constitutive model can recover different limiting cases, demonstrating its generality, and can better capture the heat and mass transfer behaviors of viscoelastic fluids.

• Numerical results reveal that the relaxation time λ and the fractional integral index β_1 suppress the convective flow, whereas the associated fractional derivative order α_1 enhances the nanofluid velocity. Moreover, increasing the permeability of the porous medium promotes fluid motion, while a

stronger magnetic field inhibits the flow. For the thermal boundary layer, the two phase-lag parameters exhibit opposite influences, and their effects under isothermal wall temperature conditions are nonmonotonic. In particular, the thermal boundary layer is more sensitive to the phase lag of the temperature gradient τ_T.

This paper is organized as follows. In Section 2, a mathematical model for viscoelastic nanofluids is formulated using the dual-parameter fractional Maxwell constitutive relation and the time-fractional DPL equation. In Section 3, the boundary layer equations are discretized and solved using the finite difference method, incorporating the L1 algorithm and the weighted-shifted Grünwald difference scheme. In Section 4, two source terms are introduced into the governing equations to validate the proposed numerical scheme. In Section 5, the effects of key parameters on nanofluid flow and thermal characteristics are analyzed. Finally, Section 6 summarizes key conclusions.

2. Mathematical formulation

We examine the transient natural convection and heat transfer of an incompressible nanofluid past an infinite vertical plate within a porous medium, shown schematically in Figure 1. A transverse magnetic field B_0 and thermal radiation q_r are applied to the system. Initially, both the plate and the nanofluid remain stationary with a uniform ambient temperature T_∞. For $t > 0$, the plate begins to move at a constant velocity u_0, while its temperature varies linearly with time as $T_\infty + (T_w - T_\infty)t/t_0$ during the interval $0 < t \le t_0$, after which it remains constant at T_w. As shown in Figure 1, the coordinate system aligns the x-axis parallel to the plate and the y-axis normal to it. Since the plate spans indefinitely along the x-axis, the controlling variables for the nanofluid flow depend solely on y and t, making the problem effectively two-dimensional. The infinite vertical plate considered here serves as an idealized benchmark geometry, which makes it possible to examine the coupled effects of viscoelastic memory, magnetic field, porous medium effects, and transient wall heating in a clear and tractable manner.

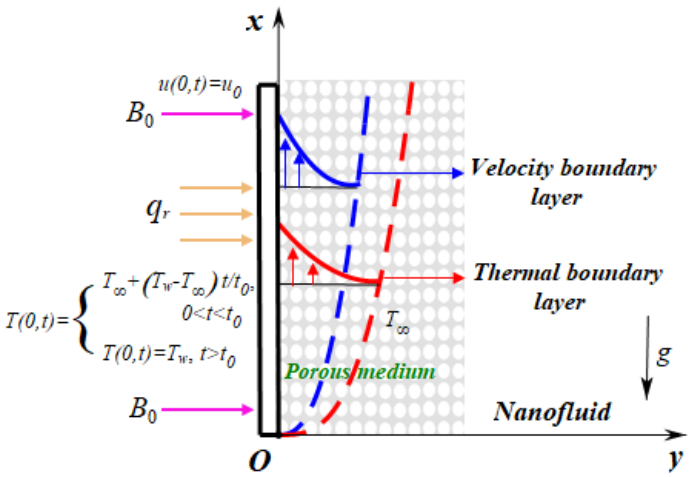

Figure 1. Diagram of the physical model.

In the present configuration, the ambient fluid is assumed to be initially quiescent and no externally imposed pressure gradient exists along the flow direction. Consequently, the flow is mainly driven

by buoyancy forces arising from temperature differences, and the pressure gradient term is neglected in the momentum equation. Fundamental assumptions governing the nanofluid model comprise: (i) Local thermal equilibrium prevails between nanoparticles and the base fluid. (ii) Nanoparticles are uniformly sized and identical in shape. (iii) Given the low magnetic Reynolds number, any induced magnetic field from fluid motion is insignificant relative to the externally imposed magnetic field. (iv) The thermophysical characteristics of the nanofluid remain invariant, aside from changes driven by the volume fraction of the nanoparticles.

2.1. Preliminary knowledge

We first recall the definition of fractional calculus, which plays an essential role in modeling the viscoelastic behavior of nanofluids.

Definition 1. *[34] For fractional order $\gamma > 0$ and any function $f \in L^1(D)$, the Riemann–Liouville fractional integral is denoted as*

$$I_t^{\gamma} f(t) = \frac{1}{\Gamma(\gamma)} \int_0^t \frac{f(\eta)\, d\eta}{(t-\eta)^{1-\gamma}}.$$

Definition 2. *[34] The γ-order Riemann–Liouville fractional derivative for any function $f \in L^1(D)$ is given by ($n-1 < \gamma < n$, $n \in \mathbb{N}$)*

$${}^{RL}D_t^{\gamma} f(t) = \frac{\mathrm{d}^n}{\mathrm{d}t^n}(I_t^{n-\gamma} f)(t) = \frac{1}{\Gamma(n-\gamma)} \frac{\mathrm{d}^n}{\mathrm{d}t^n} \int_0^t \frac{f(\eta)\, d\eta}{(t-\eta)^{1+\gamma-n}}.$$

Definition 3. *[34] The γ-order Caputo fractional derivative for any function $f \in L^1(D)$ is defined as ($n-1 < \gamma < n$, $n \in \mathbb{N}$)*

$${}^{C}D_t^{\gamma} f(t) = I_t^{n-\gamma} f^{(n)}(t) = \frac{1}{\Gamma(n-\gamma)} \int_0^t \frac{f^{(n)}(\eta)\, d\eta}{(t-\eta)^{1+\gamma-n}}.$$

For $\gamma \in (0, 1)$, it follows that

$${}^{C}D_t^{\gamma+1} f(t) = \frac{1}{\Gamma(1-\gamma)} \int_0^t \frac{f''(\eta)\, d\eta}{(t-\eta)^{\gamma}} = {}^{C}D_t^{\gamma} f'(t). \tag{2.1}$$

2.2. Fractional stress-strain constitutive relationship

The classical Maxwell constitutive equation governing the stress-strain relationship is established as

$$\sigma(t) + \tau \frac{d\sigma(\mathrm{t})}{dt} = \tau E \frac{d\varepsilon(\mathrm{t})}{dt}, \tag{2.2}$$

where $\sigma(t)$ and $\varepsilon(t)$ denote the stress and strain, respectively, and the dimensionless constant τ is the ratio of dashpot viscosity μ to spring modulus E. The Scott-Blair model [35] introduces a fractional element, effectively capturing material behavior between Hookean solids and Newtonian fluids. This model admits physical realization through hierarchical arrangements of elastic (spring) and viscous

(dashpot) elements, including trees, ladders, and fractal networks [36]. The fractional constitutive relation of the Scott-Blair element in terms of the Riemann–Liouville derivative can be expressed as

$$\sigma(t) = E\tau^{\gamma RL}D_t^{\gamma}\varepsilon(t), \quad 0 < \gamma < 1. \tag{2.3}$$

For $\gamma = 0$, Eq (2.3) reduces to Hooke's law, while for $\gamma = 1$, it recovers Newton's law. To generalize the Maxwell model, the dashpot and spring are replaced by two fractional elements, whose constitutive relations are defined as

$$\sigma_1(t) = E_1\tau_1^{\alpha RL}D_t^{\alpha}\varepsilon_1(t), \quad 0 < \alpha < 1, \tag{2.4}$$

$$\sigma_2(t) = E_2\tau_2^{\beta RL}D_t^{\beta}\varepsilon_2(t), \quad 0 < \beta < 1. \tag{2.5}$$

This leads to the dual-parameter fractional Maxwell model

$$\sigma(t) + \tau^{\alpha-\beta RL}D_t^{\alpha-\beta}\sigma(t) = E\tau^{\alpha RL}D_t^{\alpha}\varepsilon(t), \quad 0 < \alpha,\beta < 1, \tag{2.6}$$

where $\tau = \left(E_1\tau_1^{\alpha}/E_2\tau_2^{\beta}\right)^{1/(\alpha-\beta)}$ and $E = E_1(\tau_1/\tau)^{\alpha}$. Without loss of generality, taking $\alpha_1 = \alpha-\beta$, $\alpha_2 = \alpha$, Eq (2.6) can be rewritten as [37]

$$\sigma(t) + \lambda^{\alpha_1 RL}D_t^{\alpha_1}\sigma(t) = E\lambda^{\beta_1 RL}D_t^{\beta_1}\varepsilon(t), \quad 0 \le \alpha_1 \le \beta_1 \le 1, \tag{2.7}$$

where λ denotes the relaxation time. From the perspective of mechanical construction, the dual-parameter fractional Maxwell model inherently implies the condition $\alpha_1 \le \beta_1$, thereby avoiding the unphysical phenomenon of an increasing relaxation function [38] when $\alpha_1 > \beta_1$. Compared with the single-parameter fractional Maxwell model, the dual-parameter fractional Maxwell model introduces two fractional orders that provide greater flexibility in characterizing viscoelastic memory effects. Model (2.7) reduces to the classical Maxwell model when $\alpha_1 = \beta_1 = 1$. If $\alpha_1 = 0$ and $\beta_1 = 1$, it simplifies to the classical Newtonian viscosity law. Using the properties of Riemann–Liouville fractional calculus [39], the right-hand term in Eq (2.7) can be reformulated as

$${}^{RL}D_t^{\beta_1}\varepsilon(t) = I_t^{1-\beta_1}\left(\frac{d\varepsilon(t)}{dt}\right). \tag{2.8}$$

For the present problem, the constitutive relation (2.7) becomes

$$\sigma_{xy} + \lambda^{\alpha_1 RL}D_t^{\alpha_1}\sigma_{xy} = \mu\lambda^{\beta_1-1}I_t^{1-\beta_1}\left(\frac{\partial u}{\partial y}\right), \tag{2.9}$$

where u is the velocity component.

2.3. Fractional heat conduction constitutive relationship

Based on the Rosseland approximation [40], the radiation heat flux is expressed as

$$q_r = -\frac{4\sigma_{SB}}{3k_R}\frac{\partial T^4}{\partial y}, \tag{2.10}$$

where σ_{SB} indicates the Stefan–Boltzmann constant, k_R denotes the absorption coefficient, with T being the nanofluid temperature. By applying a first-order Taylor expansion to T^4 about T_∞, the radiation heat flux can be approximated as

$$q_r = -\frac{16\sigma_{SB}T_\infty^3}{3k_R}\frac{\partial T}{\partial y}. \tag{2.11}$$

Combining this with Fourier's law of heat conduction:

$$q = -k\nabla T, \tag{2.12}$$

the effective conduction–radiation heat flux can be obtained as [41]

$$q_{\text{eff}} = -\left(k + \frac{16\sigma_{SB}T_\infty^3}{3k_R}\right)\frac{\partial T}{\partial y} \equiv -k_{\text{eff}}\frac{\partial T}{\partial y}, \tag{2.13}$$

where k represents the thermal conductivity, and the effective thermal conductivity k_{eff} is defined as

$$k_{\text{eff}} = k + \frac{16\sigma_{SB}T_\infty^3}{3k_R}. \tag{2.14}$$

The DPL model accounts for microstructural interactions and relaxation effects by incorporating two relaxation parameters into both the heat flux τ_q and the temperature gradient τ_T, which are caused by thermal inertia and microstructural interactions [42]. Utilizing the Caputo fractional derivative and the fractional Taylor series expansion [43, 44] in the non-Fourier heat conduction model, the generalized DPL model has been studied by Ji et al. [45, 46]. The parameters α_2 and β_2 reflect the nonlocal behavior and memory effects in the evolution of the heat flux and temperature gradient. To maintain dimensional consistency, the time lags τ_q and τ_T are normalized as $\tau_q^{\alpha_2}$ and $\tau_T^{\beta_2}$, respectively. Accordingly, the time-fractional dual-phase-lag model in terms of the Caputo derivative is derived as

$$q(y,t) + \tau_q^{\alpha_2}{}^C D_t^{\alpha_2} q(y,t) = -k\left\{\nabla T(y,t) + \tau_T^{\beta_2}{}^C D_t^{\beta_2}\nabla T(y,t)\right\}, \quad 0 \le \alpha_2, \beta_2 \le 1. \tag{2.15}$$

Notably, when $\alpha_2 = \beta_2 = 1$, model (2.15) reduces to the classical DPL heat conduction model. The fractional Cattaneo heat conduction law and the classical Fourier law are obtained when $\tau_q \neq 0$, $\tau_T = 0$, and $\tau_q = \tau_T = 0$, respectively. Considering the effective conduction-radiation heat flux, the constitutive relation (2.15) is modified as

$$(1 + \tau_q^{\alpha_2}{}^C D_t^{\alpha_2}) q_{\text{eff}}(y,t) = -k_{\text{eff}}\left\{\nabla T(y,t) + \tau_T^{\beta_2}{}^C D_t^{\beta_2}\nabla T(y,t)\right\}. \tag{2.16}$$

This formulation captures the combined effects of thermal memory and radiation-enhanced conduction, thereby providing a more comprehensive model for heat transfer in nanofluids.

2.4. Fractional boundary layer governing equations

Based on the above hypotheses, the governing equations for the boundary layer's laminar hydromagnetic free convection flow of nanofluids are provided by [47]

$$\rho_{\text{nf}}\frac{\partial u(y,t)}{\partial t} = \frac{\partial \sigma_{xy}}{\partial y} - (\sigma_e)_{\text{nf}} B_0^2 u(y,t) - \frac{\mu_{\text{nf}}}{K'}u(y,t) + (\rho\beta_T)_{\text{nf}} g[T(y,t) - T_\infty], \tag{2.17}$$

$$(\rho C_p)_{\rm nf}\frac{\partial T\,(y,t)}{\partial t} = -\nabla q_{\rm eff} + Q_0[T\,(y,t) - T_\infty], \tag{2.18}$$

where the parameters are defined as follows:

$\rho_{\rm nf}$: nanofluid density, $\mu_{\rm nf}$: dynamic viscosity, $(\beta_T)_{\rm nf}$: volumetric coefficient of thermal expansion, $(\sigma_e)_{\rm nf}$: electrical conductivity, $\nu_{\rm nf} = (\mu/\rho)_{\rm nf}$: kinematic viscosity, $(C_p)_{\rm nf}$: isobaric heat capacity, g : gravitational acceleration, K' : permeability of medium, Q_0 : heat injection/consumption.

This study focuses on nanofluids containing spherical nanoparticles. Table 1 lists the thermophysical properties of the base fluid and nanoparticles used in this study. Water is selected as the base fluid due to its wide use in heat transfer systems, low cost, environmental compatibility, and relatively high heat capacity. The nanoparticles Cu, Ag, and TiO_2 are chosen as representative materials with distinct properties: Cu and Ag feature high thermal conductivity, whereas TiO_2 offers good chemical stability and dispersion behavior in water. These water-based nanofluids are widely used in thermal management applications such as electronic cooling, heat exchangers, and energy systems [48, 49]. The relationship between the thermophysical properties of the nanofluid and its components is described by [50]

$$\begin{aligned}
&\mu_{\rm nf} = \frac{\mu_{\rm bf}}{(1-\varphi)^{2.5}}, \quad \rho_{\rm nf} = (1-\varphi)\,\rho_{\rm bf} + \varphi\rho_{\rm np}, \quad k_{\rm nf} = k_{\rm f}\left[\frac{k_{\rm np} + 2k_{\rm bf} - 2\varphi\left(k_{\rm bf} - k_{\rm np}\right)}{k_{\rm np} + 2k_{\rm bf} + \varphi\left(k_{\rm bf} - k_{\rm np}\right)}\right],\\
&\left(\rho C_p\right)_{\rm nf} = (1-\varphi)\left(\rho C_p\right)_{\rm bf} + \varphi\left(\rho C_p\right)_{\rm np}, \quad (\rho\beta_T)_{\rm nf} = (1-\varphi)\,(\rho\beta_T)_{\rm bf} + \varphi\,(\rho\beta_T)_{\rm np},\\
&(\sigma_e)_{\rm nf} = (\sigma_e)_{\rm bf}\left[1 + \frac{3\varphi\,(\sigma'-1)}{(\sigma'+2) - \varphi\,(\sigma'-1)}\right], \quad \sigma' = \frac{(\sigma_e)_{\rm np}}{(\sigma_e)_{\rm bf}}.
\end{aligned}$$

Here, the subscripts "np", "bf", and "nf" stand for the nanoparticles, base fluid, and nanofluid, respectively, while φ represents the nanoparticle volume fraction. In nanofluids, microscopic interfacial interactions (particle-particle and particle-fluid coupling, including Brownian motion) may modify the effective thermophysical properties of the suspension, such as viscosity, thermal conductivity, and the thermal expansion coefficient. In the present model, these effects are incorporated implicitly through the effective thermophysical properties defined above, thereby influencing the flow and heat transfer behavior.

By substituting the generalized constitutive relationships (2.9) and (2.16) into Eqs (2.17) and (2.18), respectively, we derive the fractional governing boundary layer equations:

$$\begin{aligned}
\left(1 + \lambda^{\alpha_1}{}^{RL}D_t^{\alpha_1}\right)\frac{\partial u\,(y,t)}{\partial t} &= \nu_{\rm nf}\lambda^{\beta_1-1}I_t^{1-\beta_1}\left(\frac{\partial^2 u(y,t)}{\partial y^2}\right) - \left(\frac{(\sigma_e)_{\rm nf}\,B_0^2}{\rho_{\rm nf}} + \frac{\nu_{\rm nf}}{K'}\right)\left(1 + \lambda^{\alpha_1}{}^{RL}D_t^{\alpha_1}\right)u(y,t)\\
&\quad + g\,(\beta_T)_{\rm nf}\left(1 + \lambda^{\alpha_1}{}^{RL}D_t^{\alpha_1}\right)[T(y,t) - T_\infty],
\end{aligned} \tag{2.19}$$

$$\left(1 + \tau_q^{\alpha_2}{}^{C}D_t^{\alpha_2}\right)\frac{\partial T\,(y,t)}{\partial t} = \frac{k_{\rm eff}}{(\rho C_p)_{\rm nf}}\left(1 + \tau_T^{\beta_2}{}^{C}D_t^{\beta_2}\right)\frac{\partial^2 T(y,t)}{\partial y^2} + \frac{Q_0}{(\rho C_p)_{\rm nf}}\left(1 + \tau_q^{\alpha_2}{}^{C}D_t^{\alpha_2}\right)[T(y,t) - T_\infty]. \tag{2.20}$$

The initial and boundary conditions are prescribed according to the physical setup of the present problem and the standard assumptions of transient free-convection boundary-layer theory with ramped wall heating. Thus, the governing equations are supplemented by the following initial and boundary conditions [51, 52]:

$$u(y,0) = 0,\ T(y,0) = T_\infty, \quad y \geq 0, \tag{2.21}$$

$$u(0,t) = u_0, \quad t > 0, \tag{2.22}$$

$$T(0,t) = \begin{cases} T_\infty + (T_w - T_\infty)t/t_0, & 0 < t \leq t_0, \\ T_w, & t > t_0, \end{cases} \tag{2.23}$$

$$\lim_{y\to+\infty} u(y,t) = 0,\ \lim_{y\to+\infty} T(y,t) = T_\infty. \tag{2.24}$$

To preserve dimensional homogeneity in the proposed nanofluid model, the dimensionless quantities are defined as

$$y^* = \frac{u_0}{\nu_{\rm bf}}y, \quad u^* = \frac{1}{u_0}u, \quad t^* = \frac{u_0^2}{\nu_{\rm bf}}t, \quad \lambda^* = \frac{u_0^2}{\nu_{\rm bf}}\lambda,$$
$$\tau_q^* = \frac{u_0^2}{\nu_{\rm bf}}\tau_q, \quad \tau_T^* = \frac{u_0^2}{\nu_{\rm bf}}\tau_T, \quad T^* = \frac{T - T_\infty}{T_w - T_\infty}.$$

To ensure consistency in the nondimensionalization process, the reference time t_0 may be specified as $\nu_{\rm bf}/u_0^2$. By substituting these expressions into the governing equations (2.19) and (2.20) and omitting the dimensionless notation "*", we derive the dimensionless governing equations:

$$\left(1 + \lambda^{\alpha_1 RL}D_t^{\alpha_1}\right)\frac{\partial u(y,t)}{\partial t} = \frac{\varphi_4}{\varphi_1}\lambda^{\beta_1-1}I_t^{1-\beta_1}\left(\frac{\partial^2 u(y,t)}{\partial y^2}\right) - \left(\frac{\varphi_6 B}{\varphi_1} + \frac{\varphi_4}{\varphi_1 K}\right)\left(1 + \lambda^{\alpha_1 RL}D_t^{\alpha_1}\right)u(y,t)$$
$$+ \varphi_2 Gr\left(1 + \lambda^{\alpha_1 RL}D_t^{\alpha_1}\right)T(y,t), \tag{2.25}$$

$$\left(1 + \tau_q^{\alpha_2 C}D_t^{\alpha_2}\right)\frac{\partial T(y,t)}{\partial t} = \frac{\varphi_5 + Nr}{\varphi_3 Pr}\left(1 + \tau_T^{\beta_2 C}D_t^{\beta_2}\right)\frac{\partial^2 T(y,t)}{\partial y^2} + \frac{Q}{\varphi_3}\left(1 + \tau_q^{\alpha_2 C}D_t^{\alpha_2}\right)T(y,t). \tag{2.26}$$

Here, the dimensionless parameters are defined as follows:

$$Gr = \frac{g(\beta_T\nu)_{\rm bf}(T_w - T_\infty)}{u_0^3}, \quad B = \frac{B_0^2}{u_0^2}\left(\frac{\sigma_e\nu}{\rho}\right)_{\rm bf}, \quad K = \frac{K'u_0^2}{\nu_{\rm bf}^2},$$
$$Nr = \frac{16\sigma_{SB}T_\infty^3}{3k_{\rm bf}k_R}, \quad Pr = \left(\frac{\rho C_p\nu}{k}\right)_{\rm bf}, \quad Q = \frac{Q_0}{u_0^2}\left(\frac{\nu}{\rho C_p}\right)_{\rm bf}.$$

The dimensionless parameters are interpreted as follows: Gr denotes the Grashof number, B represents the magnetic parameter, K is the permeability parameter, Nr denotes the thermal radiation parameter, Pr represents the Prandtl number, and Q is the heat injection/consumption parameter. The coefficients $\varphi_i\,(i = 1, 2, \cdots, 6)$ are dimensionless functions derived from the thermophysical characteristics of the base fluid and nanoparticles:

$$\varphi_1 = (1-\varphi) + \varphi\left(\frac{\rho_{\rm np}}{\rho_{\rm bf}}\right), \quad \varphi_2 = \frac{(1-\varphi)\rho_{\rm bf} + \varphi\rho_{\rm np}\frac{(\beta_T)_{\rm np}}{(\beta_T)_{\rm bf}}}{\rho_{\rm nf}}, \quad \varphi_3 = (1-\varphi) + \varphi\frac{\left(\rho C_p\right)_{\rm np}}{\left(\rho C_p\right)_{\rm bf}},$$

$$\varphi_4 = \frac{1}{(1-\varphi)^{2.5}}, \quad \varphi_5 = \frac{k_{\rm np} + 2k_{\rm bf} - 2\varphi\left(k_{\rm bf} - k_{\rm np}\right)}{k_{\rm np} + 2k_{\rm bf} + \varphi\left(k_{\rm bf} - k_{\rm np}\right)}, \quad \varphi_6 = \left[1 + \frac{3\varphi\,(\sigma' - 1)}{(\sigma' + 2) - \varphi\,(\sigma' - 1)}\right].$$

The dimensionless initial and boundary conditions are determined as

$$u(y,0) = 0,\ T(y,0) = 0, \quad y \geq 0, \tag{2.27}$$

$$u(0,t) = 1, \quad t > 0, \tag{2.28}$$

$$T\,(0,t) = \begin{cases} t, & 0 < t \leq 1, \\ 1, & t > 1, \end{cases} \tag{2.29}$$

$$\lim_{\rm y\to+\infty} u\,(y,t) = 0,\ \lim_{\rm y\to+\infty} T\,(y,t) = 0. \tag{2.30}$$

Table 1. Thermophysical characteristics of the base fluid and nanoparticles.

Fluid/nanoparticles	ρ (kg · m^{-3})	C_p (J · kg^{-1} · K^{-1})	k (W · m^{-1} · K^{-1})	$\beta_T \times 10^5$ (K^{-1})	σ_e (S · m^{-1})
Water	997.1	4179	0.613	21	5.5×10^{-6}
Copper (Cu)	8933	385	401	1.67	5.96×10^{7}
Silver (Ag)	10500	235	429	1.89	6.3×10^{7}
Titanium oxide (TiO_2)	4250	686.2	8.9538	0.90	2.6×10^{6}

3. Numerical technique

In this section, we present the finite difference scheme for solving the governing equations (2.25)–(2.30). The L1 algorithm and the weighted-shifted Grünwald difference scheme are employed to discretize the fractional-order operators appearing in the model. We first introduce the discretization of the computational domain, then describe the approximations for time-fractional derivatives and for mixed derivative terms, and finally give the fully discrete scheme together with its truncation error.

3.1. Discretization of the computational domain

For the spatial domain $[0, L]$, we define uniform grid points $y_i = i\Delta y$ with $i = 0, 1, \ldots, M$, where $\Delta y = L/M$ is the spatial step size. For the temporal domain $[0, t_{\rm total}]$, we set $t_n = n\Delta t$ with $n = 0, 1, \ldots, N$ and $\Delta t = t_{\rm total}/N$. For any grid function $u_i^n = u(y_i, t_n)$ and $T_i^n = T(y_i, t_n)$, we introduce the following notations:

$$\nabla_t u_i^n = \frac{u_i^n - u_i^{n-1}}{\Delta t}, \qquad \nabla_t T_i^n = \frac{T_i^n - T_i^{n-1}}{\Delta t},$$

$$\delta_y^2 u_i^n = \frac{u_{i-1}^n - 2u_i^n + u_{i+1}^n}{(\Delta y)^2}, \qquad \delta_y^2 T_i^n = \frac{T_{i-1}^n - 2T_i^n + T_{i+1}^n}{(\Delta y)^2}.$$

The integer-order derivatives at (y_i, t_n) are approximated by

$$\frac{\partial u(y_i,t_n)}{\partial t} = \nabla_t u_i^n + O(\Delta t), \quad \frac{\partial T(y_i,t_n)}{\partial t} = \nabla_t T_i^n + O(\Delta t), \quad \frac{\partial^2 T(y_i,t_n)}{\partial y^2} = \delta_y^2 T_i^n + O((\Delta y)^2).$$

3.2. Discretization of time-fractional derivatives

The Caputo time-fractional derivatives are approximated by the L1 algorithm. For the order $\alpha_2 \in (0, 1)$, we have

$$
\begin{aligned}
{}^{C}D_t^{\alpha_2} T(y_i, t_n) &= \frac{(\Delta t)^{-\alpha_2}}{\Gamma(2-\alpha_2)}\left[a_0^{(\alpha_2)} T_i^n - \sum_{k=1}^{n-1} (a_{n-k-1}^{(\alpha_2)} - a_{n-k}^{(\alpha_2)}) T_i^k - a_{n-1}^{(\alpha_2)} T_i^0\right] + O((\Delta t)^{2-\alpha_2}) \qquad (3.1)\\
&= \frac{(\Delta t)^{1-\alpha_2}}{\Gamma(2-\alpha_2)} \sum_{k=1}^{n} a_{n-k}^{(\alpha_2)} \nabla_t T_i^k + O((\Delta t)^{2-\alpha_2}),
\end{aligned}
$$

where $a_k^{(\alpha_2)} = (k+1)^{1-\alpha_2} - k^{1-\alpha_2}$, $k = 0, 1, \ldots, n-1$. For the order $\alpha_2 + 1 \in (1, 2)$, the L1 discretization based on Eq (2.1) yields

$$
{}^{C}D_t^{\alpha_2+1} T(y_i, t_n) = \frac{(\Delta t)^{-\alpha_2}}{\Gamma(2-\alpha_2)}\left[a_0^{(\alpha_2)} \nabla_t T_i^n - \sum_{k=1}^{n-1} (a_{n-k-1}^{(\alpha_2)} - a_{n-k}^{(\alpha_2)}) \nabla_t T_i^k - a_{n-1}^{(\alpha_2)} \nabla_t T_i^0\right] + O(\Delta t), \qquad (3.2)
$$

with $T_i^{-1} = T_i^0 - \Delta t \frac{\partial T(y_i, 0)}{\partial t}$.

The following lemma is introduced to discretize the Riemann–Liouville time-fractional derivative.

Lemma 1. *[53] For $n - 1 < \alpha \le n$, $n \in \mathbb{N}$, and $f \in AC^n(\overline{D})$,*

$$
{}^{RL}D_t^{\alpha} f(t) = {}^{C}D_t^{\alpha} f(t) + \sum_{j=0}^{n-1} \frac{f^{(j)}(0)\, t^{j-\alpha}}{\Gamma(1+j-\alpha)},
$$

where $AC^n(\overline{D}) := \{f : f^{(n)} \in L^1(D)\}$. If $f^{(j)}(0) = 0$ for $j = 0, 1, \ldots, n-1$, the Caputo and Riemann–Liouville derivatives coincide.

Owing to the homogeneous initial conditions (2.27), the Riemann–Liouville derivatives ${}^{RL}D_t^{\alpha_1} u(y_i, t_n)$, ${}^{RL}D_t^{\alpha_1} T(y_i, t_n)$, and ${}^{RL}D_t^{\alpha_1+1} u(y_i, t_n)$ can be discretized by the L1 scheme.

3.3. Discretization of mixed derivative terms

The coupling between fractional operators and spatial derivatives is treated by the weighted-shifted Grünwald approximation.

Lemma 2. *[54] (i) For $\gamma > 0$, let $f \in L^1(\mathbb{R})$ with $I_t^{\gamma-2} f(t)$ and $(\mathrm{i}\omega)^{2-\gamma} \mathcal{F}[f](\omega) \in L^1(\mathbb{R})$. Define the weighted-shifted Grünwald difference scheme as follows:*

$$
\begin{aligned}
\mathcal{I}_{\Delta t,p,q}^{\gamma} f(t) = \frac{(\Delta t)^{\gamma}}{2(q-p)}\Big[&(\gamma + 2q) \sum_{k=0}^{\infty} (-1)^k \binom{-\gamma}{k} f(t - (k-p)\Delta t)\\
&- (2p + \gamma) \sum_{k=0}^{\infty} (-1)^k \binom{-\gamma}{k} f(t - (k-q)\Delta t)\Big],
\end{aligned}
$$

with $p, q \in \mathbb{Z}$, $p \ne q$. Then $\mathcal{I}_{\Delta t,p,q}^{\gamma} f(t) = I_t^{\gamma} f(t) + O((\Delta t)^2)$ for $t \in \mathbb{R}$.

(ii) For the Riemann–Liouville derivative,

$$ {}^{RL}\mathcal{D}^{\gamma}_{\Delta t,p,q} f(t) = \frac{(\Delta t)^{-\gamma}}{2(p-q)}\Big[(\gamma-2q)\sum_{k=0}^{\infty}(-1)^k\binom{\gamma}{k} f(t-(k-p)\Delta t) + (2p-\gamma)\sum_{k=0}^{\infty}(-1)^k\binom{\gamma}{k} f(t-(k-q)\Delta t)\Big] $$

satisfies ${}^{RL}\mathcal{D}^{\gamma}_{\Delta t,p,q} f(t) = {}^{RL}D^{\gamma}_{t} f(t) + O((\Delta t)^2)$, $t \in \mathbb{R}$.

Taking $(p, q) = (0, -1)$ in Lemma 2 yields for the fractional integral in the momentum equation

$$ \begin{aligned} I_t^{1-\beta_1}\left(\frac{\partial^2 u}{\partial y^2}\right)(y_i, t_n) &= (\Delta t)^{1-\beta_1}\left[\frac{1+\beta_1}{2}\sum_{k=0}^{n}\omega_k^{(1-\beta_1)}\delta_y^2 u_i^{n-k} + \frac{1-\beta_1}{2}\sum_{k=0}^{n-1}\omega_k^{(1-\beta_1)}\delta_y^2 u_i^{n-k-1}\right] + O((\Delta t)^2 + (\Delta y)^2) \\ &= (\Delta t)^{1-\beta_1}\sum_{k=0}^{n}\gamma_k^{(\beta_1)}\delta_y^2 u_i^{n-k} + O((\Delta t)^2 + (\Delta y)^2), \end{aligned} \tag{3.3} $$

where $\omega_k^{(1-\beta_1)} = (-1)^k\binom{\beta_1-1}{k}$, and

$$ \gamma_0^{(\beta_1)} = \tfrac{1+\beta_1}{2}\omega_0^{(1-\beta_1)}, \quad \gamma_k^{(\beta_1)} = \tfrac{1+\beta_1}{2}\omega_k^{(1-\beta_1)} + \tfrac{1-\beta_1}{2}\omega_{k-1}^{(1-\beta_1)} \ (k \geq 1). $$

Similarly, for the Caputo derivative in the temperature equation, we obtain

$$ \begin{aligned} {}^{C}D_t^{\beta_2}\left(\frac{\partial^2 T}{\partial y^2}\right)(y_i, t_n) &= (\Delta t)^{-\beta_2}\left[\frac{2+\beta_2}{2}\sum_{k=0}^{n} g_k^{(\beta_2)}\delta_y^2 T_i^{n-k} - \frac{\beta_2}{2}\sum_{k=0}^{n-1} g_k^{(\beta_2)}\delta_y^2 T_i^{n-k-1}\right] + O((\Delta t)^2 + (\Delta y)^2) \\ &= (\Delta t)^{-\beta_2}\sum_{k=0}^{n}\lambda_k^{(\beta_2)}\delta_y^2 T_i^{n-k} + O((\Delta t)^2 + (\Delta y)^2), \end{aligned} \tag{3.4} $$

with $g_k^{(\beta_2)} = (-1)^k\binom{\beta_2}{k}$, and

$$ \lambda_0^{(\beta_2)} = \tfrac{2+\beta_2}{2} g_0^{(\beta_2)}, \quad \lambda_k^{(\beta_2)} = \tfrac{2+\beta_2}{2} g_k^{(\beta_2)} - \tfrac{\beta_2}{2} g_{k-1}^{(\beta_2)} \ (k \geq 1). $$

3.4. Fully discrete scheme

Substituting the above approximations into the governing equations yields the following discrete scheme:

$$ \begin{aligned} &\nabla_t u_i^n + \lambda^{\alpha_1}\frac{(\Delta t)^{-\alpha_1}}{\Gamma(2-\alpha_1)}\left[a_0^{(\alpha_1)}\nabla_t u_i^n - \sum_{k=1}^{n-1}(a_{n-k-1}^{(\alpha_1)} - a_{n-k}^{(\alpha_1)})\nabla_t u_i^k - a_{n-1}^{(\alpha_1)}\nabla_t u_i^0\right] \\ &= \frac{\varphi_4}{\varphi_1}\lambda^{\beta_1-1}(\Delta t)^{1-\beta_1}\sum_{k=0}^{n}\gamma_k^{(\beta_1)}\delta_y^2 u_i^{n-k} - \left(\frac{\varphi_6 B}{\varphi_1} + \frac{\varphi_4}{\varphi_1 K}\right)\left[u_i^n + \lambda^{\alpha_1}\frac{(\Delta t)^{1-\alpha_1}}{\Gamma(2-\alpha_1)}\sum_{k=1}^{n} a_{n-k}^{(\alpha_1)}\nabla_t u_i^k\right] \\ &\quad + \varphi_2 Gr\left[T_i^n + \lambda^{\alpha_1}\frac{(\Delta t)^{1-\alpha_1}}{\Gamma(2-\alpha_1)}\sum_{k=1}^{n} a_{n-k}^{(\alpha_1)}\nabla_t T_i^k\right], \end{aligned} \tag{3.5} $$

$$\nabla_t T_i^n + \tau_q^{\alpha_2} \frac{(\Delta t)^{-\alpha_2}}{\Gamma(2-\alpha_2)} \left[a_0^{(\alpha_2)} \nabla_t T_i^n - \sum_{k=1}^{n-1} (a_{n-k-1}^{(\alpha_2)} - a_{n-k}^{(\alpha_2)}) \nabla_t T_i^k - a_{n-1}^{(\alpha_2)} \nabla_t T_i^0 \right]$$
$$= \frac{\varphi_5 + Nr}{\varphi_3 Pr} \delta_y^2 T_i^n + \frac{\varphi_5 + Nr}{\varphi_3 Pr} \tau_T^{\beta_2} (\Delta t)^{-\beta_2} \sum_{k=0}^{n} \lambda_k^{(\beta_2)} \delta_y^2 T_i^{n-k} + \frac{Q}{\varphi_3} T_i^n$$
$$+ \frac{Q}{\varphi_3} \tau_q^{\alpha_2} \frac{(\Delta t)^{1-\alpha_2}}{\Gamma(2-\alpha_2)} \sum_{k=1}^{n} a_{n-k}^{(\alpha_2)} \nabla_t T_i^k, \tag{3.6}$$

where the truncation error is of order $O(\Delta t + (\Delta y)^2)$. Due to the nonlocal nature of fractional operators, the evaluation of the L1 formula and the weighted-shifted Grünwald difference scheme requires convolution sums over all previous time levels. Consequently, the computational cost scales approximately as $O(N^2)$ with respect to the number of time steps N, while the memory requirement scales as $O(N)$. This reflects the inherent history dependence of fractional derivatives.

The dimensionless initial and boundary conditions are discretized as

$$u_i^0 = 0,\ T_i^0 = 0,\ 0 \le i \le M;$$
$$u_0^n = 1,\ T_0^n = \begin{cases} t_n, & 0 < t_n \le 1, \\ 1, & t_n > 1, \end{cases},\ u_M^n = 0,\ T_M^n = 0, \quad 1 \le n \le N.$$

The governing momentum and energy transport equations are embedded directly into the finite difference discretization framework, ensuring that the numerical solutions satisfy the underlying physical transport mechanisms and improving the overall accuracy of the computed velocity and temperature fields.

4. Numerical validation and model comparison

In this section, numerical experiments are conducted to verify the accuracy and reliability of the proposed numerical scheme. First, the method of manufactured solutions is employed to examine the convergence behavior and error characteristics of the scheme. Then, the present model is compared with several classical and fractional nanofluid models to further demonstrate the consistency of the numerical results.

4.1. Numerical validation and error analysis

To validate the accuracy of the proposed numerical scheme, the method of manufactured solutions is employed. By introducing two artificial source terms $g_1(y,t)$ and $g_2(y,t)$ into the governing equations (2.25) and (2.26), exact solutions for the velocity and temperature fields can be constructed within the computational domain $(y,t) \in [0,1] \times [0, t_{\text{total}}]$. This approach allows a quantitative assessment of the numerical errors and convergence behavior of the proposed finite difference scheme. The modified governing equations with the source terms take the form

$$\frac{\partial u(y,t)}{\partial t} + \lambda^{\alpha_1} \frac{\partial^{\alpha_1+1} u(y,t)}{\partial t^{\alpha_1+1}} = \frac{\varphi_4}{\varphi_1} \lambda^{\beta_1 - 1} I_t^{1-\beta_1} \left(\frac{\partial^2 u(y,t)}{\partial y^2} \right) - \left(\frac{\varphi_6 B}{\varphi_1} + \frac{\varphi_4}{\varphi_1 K} \right) \left(1 + \lambda^{\alpha_1} \frac{\partial^{\alpha_1}}{\partial t^{\alpha_1}} \right) u(y,t)$$
$$+ \varphi_2 Gr \left(1 + \lambda^{\alpha_1} \frac{\partial^{\alpha_1}}{\partial t^{\alpha_1}} \right) T(y,t) + g_1(y,t), \tag{4.1}$$

$$\frac{\partial T(y,t)}{\partial t}+\tau_q^{\alpha_2}\frac{\partial^{\alpha_2+1}T(y,t)}{\partial t^{\alpha_2+1}}=\frac{\varphi_5+Nr}{\varphi_3 Pr}\left(1+\tau_T^{\beta_2}\frac{\partial^{\beta_2}}{\partial t^{\beta_2}}\right)\frac{\partial^2 T(y,t)}{\partial y^2}+\frac{Q}{\varphi_3}\left(1+\tau_q^{\alpha_2}\frac{\partial^{\alpha_2}}{\partial t^{\alpha_2}}\right)T(y,t)+g_2(y,t), \tag{4.2}$$

along with the initial and boundary conditions

$$u(y,0)=1,\ T(y,0)=1; \tag{4.3}$$

$$u(0,t)=1,\ u(1,t)=1,\ T(0,t)=1,\ T(1,t)=1. \tag{4.4}$$

The exact solutions are assumed as

$$u(y,t)=y(1-y)t^2+1,\ T(y,t)=y(1-y)t^2+1.$$

By substituting these solutions into the modified governing equations, we determine the required source:

$$\begin{aligned}g_1(y,t)=&\,y(1-y)\left[2t+\frac{2\lambda^{\alpha_1}t^{1-\alpha_1}}{\Gamma(2-\alpha_1)}\right]+\left(\frac{\varphi_6 B}{\varphi_1}+\frac{\varphi_4}{\varphi_1 K}-\varphi_2 Gr\right)\left[y(1-y)t^2+1\right]\\&+\frac{4\varphi_4\lambda^{\beta_1-1}t^{3-\beta_1}}{\varphi_1\Gamma(4-\beta_1)}+\left(\frac{\varphi_6 B}{\varphi_1}+\frac{\varphi_4}{\varphi_1 K}-\varphi_2 Gr\right)\lambda^{\alpha_1}y(1-y)\frac{2t^{2-\alpha_1}}{\Gamma(3-\alpha_1)},\end{aligned}$$

$$\begin{aligned}g_2(y,t)=&\,y(1-y)\left[2t+\frac{2\tau_q^{\alpha_2}t^{1-\alpha_2}}{\Gamma(2-\alpha_2)}\right]+\frac{2(\varphi_5+Nr)t^2}{\varphi_3 Pr}+\frac{4(\varphi_5+Nr)\tau_T^{\beta_2}t^{2-\beta_2}}{\varphi_3 Pr\Gamma(3-\beta_2)}\\&-\frac{Q}{\varphi_3}\left[y(1-y)t^2+1\right]-\frac{Q}{\varphi_3}\tau_q^{\alpha_2}y(1-y)\frac{2t^{2-\alpha_2}}{\Gamma(3-\alpha_2)}.\end{aligned}$$

The source terms are constructed consistently with the governing equations so that the difference between the Riemann–Liouville and Caputo derivatives does not influence the numerical verification. The numerical solutions obtained using the proposed scheme are then compared with the exact solutions to evaluate the accuracy of the numerical method.

Table 2. L^∞ errors and convergence orders for $u(y,t)$ and $T(y,t)$.

	u		T	
Δt	Error	Order	Error	Order
1/10	2.9426×10^{-3}	–	1.0318×10^{-2}	–
1/20	1.4955×10^{-3}	0.976	5.2074×10^{-3}	0.987
1/40	7.5146×10^{-4}	0.993	2.6183×10^{-3}	0.992
1/80	3.7646×10^{-4}	0.997	1.3136×10^{-3}	0.995
1/160	1.8845×10^{-4}	0.998	6.5820×10^{-4}	0.997

In the calculation, the parameters are chosen as $\lambda=0.2$, $B=2$, $K=0.5$, $Gr=7$, $\tau_q=0.2$, $\tau_T=0.2$, $Nr=0.75$, $Pr=6.8$, $Q=0.5$, $\alpha_1=0.2$, $\alpha_2=0.4$, $\beta_1=0.3$, $\beta_2=0.5$, and $t_{\text{total}}=1$. Table 2

lists the L^{∞} errors and the corresponding temporal convergence orders for both the velocity and temperature fields at $t = 1$ with $\Delta y = 1/800$. As the time step Δt decreases, the numerical errors reduce and the temporal convergence order approaches first order, which is consistent with the truncation error analysis presented in Section 3. These results confirm that the proposed numerical scheme achieves the expected first-order temporal accuracy. Figure 2 further compares the numerical and exact solutions, showing excellent agreement over the computational domain. The results demonstrate that the developed numerical scheme is robust and suitable for solving the present fractional governing equations. All computations were performed using MATLAB R2016a on a LENOVO laptop equipped with an AMD Ryzen 5 3500U CPU (2.10 GHz) and 8 GB RAM.

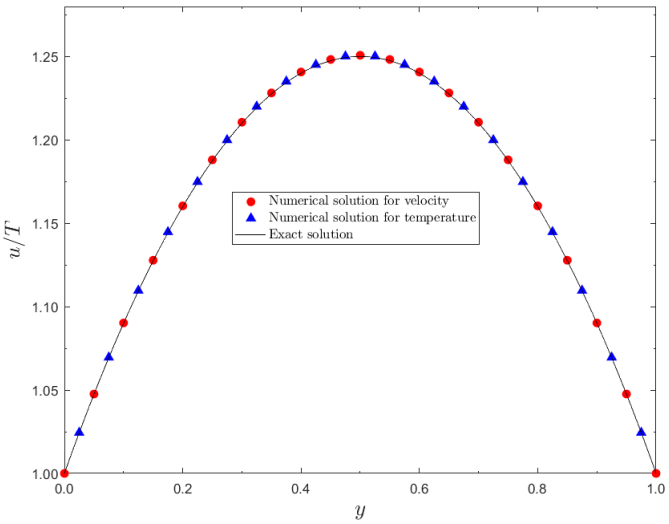

Figure 2. Comparison between the numerical and exact solutions at $t = 1$ with $\Delta y = 1/800$, $\Delta t = 1/40$.

4.2. Comparison of different nanofluid models

To further confirm the reliability of the numerical results, the present model is compared with several classical and fractional nanofluid models. Figure 3 illustrates the velocity and temperature distributions predicted by four representative models. As demonstrated in Section 2, the proposed fractional constitutive relations can recover several classical models through appropriate parameter selections. When $\alpha_1 = 0.3$ and $\beta_1 = 0.7$, Eq (2.7) corresponds to the dual-parameter fractional Maxwell model, while setting $\beta_1 = 1$ reduces it to the single-parameter fractional Maxwell model. The limiting cases $\alpha_1 = \beta_1 = 1$ and $\alpha_1 = 0$, $\beta_1 = 1$ recover the classical Maxwell model and the Newtonian viscous law, respectively. Similarly, when $\alpha_2 = 0.8$ and $\beta_2 = 0.8$, Eq (2.15) represents the fractional DPL heat conduction model, which reduces to the fractional Cattaneo law when $\tau_T = 0$. The classical DPL and Fourier laws are obtained when $\alpha_2 = \beta_2 = 1$ and $\tau_T = \tau_q = 0$, respectively.

As shown in Figure 3(a), the velocity boundary layer is thinnest in the classical Newtonian model due to the absence of viscoelastic memory effects, resulting in more direct momentum diffusion. The single-parameter fractional Maxwell nanofluid model yields a velocity profile whose thickness lies between those of the classical Newtonian and ordinary Maxwell models, reflecting the viscoelastic

memory introduced by the fractional derivative. Furthermore, the velocity boundary layer is thickest in the dual-parameter fractional Maxwell nanofluid model, indicating that the inclusion of two fractional orders enhances the viscoelastic memory characteristics and provides greater flexibility in describing the rheological behavior of complex fluids.

Regarding the temperature field, Figure 3(b) shows that the thermal boundary layer thickness exhibits relatively small differences among the classical Fourier model, the ordinary DPL model, the fractional Cattaneo model, and the fractional DPL model. The classical Fourier nanofluid model displays the largest thermal boundary layer thickness. When the phase-lag effects are introduced, as in the classical DPL model, the thermal boundary layer becomes slightly thinner. A further reduction is observed in the fractional DPL nanofluid model, while the fractional Cattaneo nanofluid model exhibits the thinnest thermal boundary layer. These results indicate that both phase-lag parameters and fractional-order effects influence the heat conduction process by modifying the temporal memory and nonlocal characteristics of thermal transport.

Overall, the results demonstrate that the proposed numerical scheme is robust and suitable for solving the present fractional governing equations. The degenerated classical models exhibit physical behaviors consistent with the results in [55], which further supports the validity of the proposed governing equations and the reliability of the numerical method.

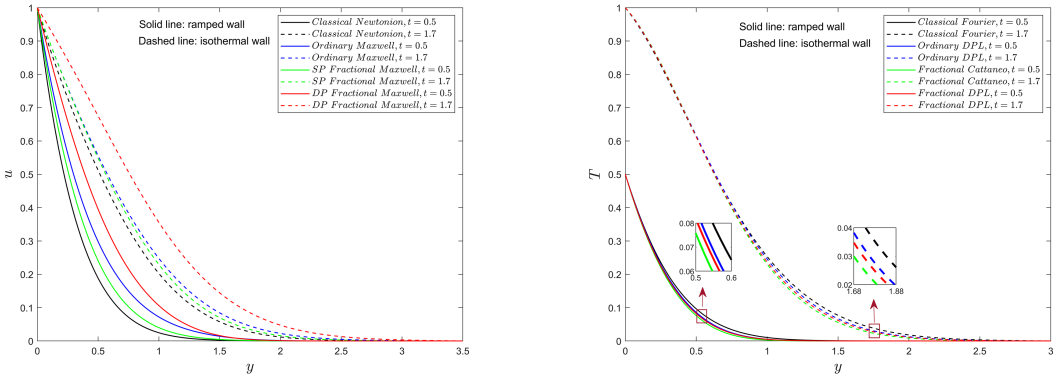

(a) Effects of different models on u

(b) Effects of different models on T

Figure 3. Velocity and temperature distributions for different models where (a) $\lambda = 0.05$, $B = 0.5$, $K = 0.15$, and $Gr = 7$; (b) $\tau_q = 0.05$, $\tau_T = 0.01$, $Nr = 0.75$, $Pr = 6.8$, and $Q = 0.5$.

5. Results and discussion

To obtain a comprehensive understanding of the physical mechanisms governing the present problem, a parametric analysis is conducted. These results not only illustrate the mathematical behavior of the proposed fractional model, but also provide insights into how viscoelastic memory effects and phase-lag heat conduction influence the momentum and thermal transport processes in nanofluid systems. Such findings are relevant for engineering applications involving complex fluid transport and heat transfer, including thermal management systems, porous medium flows, and

microscale heat transfer processes.

The flow characteristics are illustrated graphically under both ramped and isothermal wall temperature conditions, where solid lines represent the solutions for ramped wall temperature, while dashed lines correspond to the isothermal wall temperature condition. The subsequent figures systematically illustrate the effects of various parameters on the dimensionless velocity and temperature distributions. Specifically, the analysis focuses on the effects of fractional orders $(\alpha_i, \beta_i, i = 1, 2)$, relaxation time (λ), phase lags (τ_q, τ_T), the heat injection/consumption parameter (Q), the Grashof number (Gr), the Prandtl number (Pr), the radiation parameter (Nr), the magnetic parameter (B), the permeability parameter (K), time (t), the nanoparticle volume fraction (φ), and different nanoparticle types (Cu, Ag, TiO_2).

5.1. Effects on the velocity distribution

Figure 4 illustrates the influences of the fractional derivative order α_1 and integral index β_1 on the velocity distribution. An increase in α_1 results in a thicker velocity boundary layer under both ramped and isothermal wall temperature conditions (see Figure 4(a)). Conversely, the influence of β_1 is entirely opposite and more pronounced (see Figure 4(b)). Figure 5(a) shows the behavior of the velocity distribution for variations in the relaxation parameter λ. It is evident that the velocity boundary layer thickness reduces as λ rises. A similar trend manifests in the magnetic parameter B, where an increase in B results in a thinner velocity boundary layer (see Figure 5(b)). This occurs because the applied magnetic field generates a Lorentz force opposing the fluid motion, significantly reducing the nanofluid velocity. The variation of the velocity distribution with respect to the Grashof number Gr is depicted in Figure 6(a). An increase in Gr leads to a thicker velocity boundary layer, with a more pronounced effect under isothermal wall temperature conditions compared to ramped wall temperature conditions. Figure 6(b) reveals that higher permeability parameter K enhances the velocity profile. Notably, the velocity boundary layer exhibits high sensitivity to variations in K.

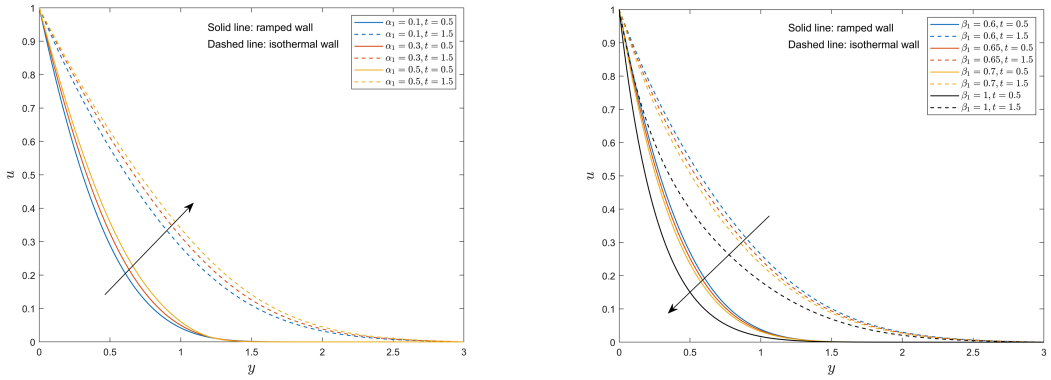

(a) Effects of α_1 **(b)** Effects of β_1

Figure 4. Velocity distribution for the fractional derivative order α_1 ($\beta_1 = 0.5$) and the fractional integral index β_1 ($\alpha_1 = 0.2$) for fixed $\lambda = 0.1$, $B = 2$, $K = 0.1$, and $Gr = 7$.

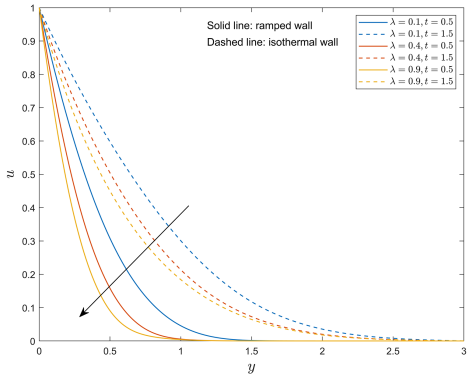

(a) Effects of λ

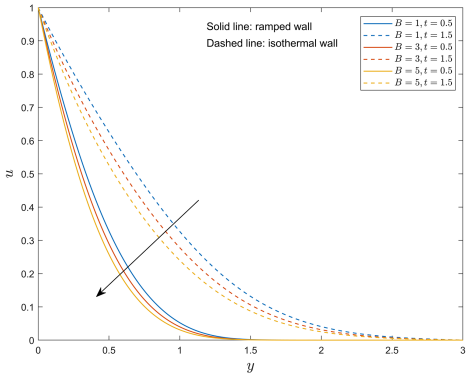

(b) Effects of B

Figure 5. Velocity distribution for the relaxation time λ ($B = 2$) and the magnetic parameter B ($\lambda = 0.1$) for fixed $\alpha_1 = 0.2, \beta_1 = 0.5$, $K = 0.1$, and $Gr = 7$.

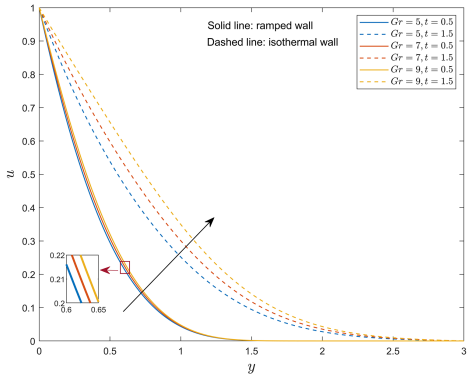

(a) Effects of Gr

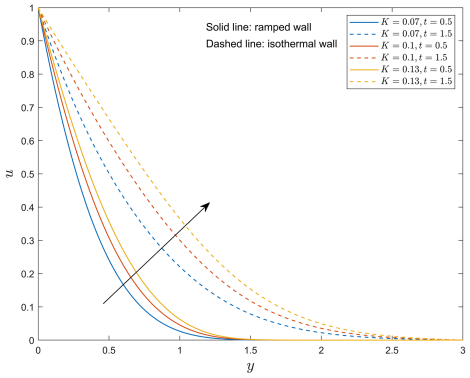

(b) Effects of K

Figure 6. Velocity distribution for the Grashof number Gr ($K = 0.1$) and the permeability parameter K ($Gr = 7$) for fixed $\lambda = 0.1$, $\alpha_1 = 0.2, \beta_1 = 0.5$, and $B = 2$.

5.2. Effects on the temperature distribution

Figure 7(a) describes the impact of the fractional derivative order α_2 on the temperature profile. The thermal boundary layer thickness increases with increasing α_2. Conversely, the fractional derivative order β_2 exhibits an opposite trend, as shown in Figure 7(b). Figure 8 presents the effects of the time-lag parameters related to heat flux τ_q and temperature gradient τ_T on the temperature distribution. Under isothermal wall temperature conditions, the thickness of the thermal boundary layer initially increases with τ_q up to a critical point ($y < 0.5$), beyond which it decreases. However, under ramped wall temperature conditions, the effect of τ_q is monotonic such that increasing τ_q reduces the thermal boundary layer thickness (see Figure 8(a)). In contrast, τ_T exhibits the opposite effect and demonstrates greater sensitivity (see Figure 8(b)).

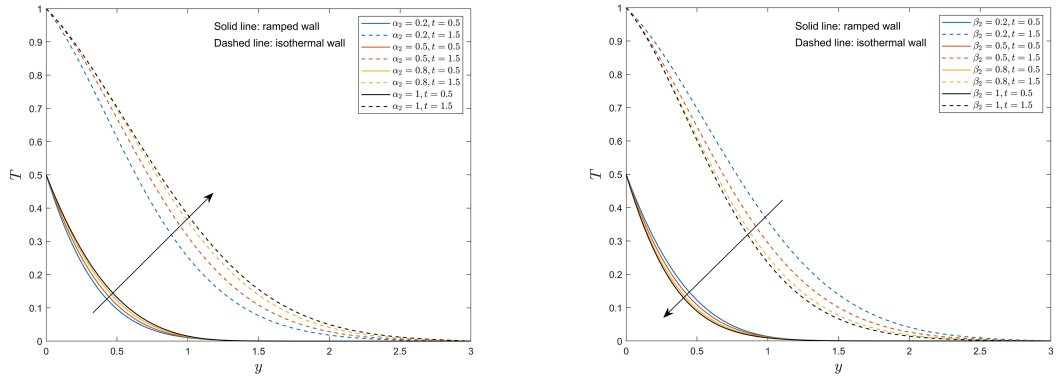

(a) Effects of α_2 **(b)** Effects of β_2

Figure 7. Temperature distribution for the fractional derivative order α_2 ($\beta_2 = 0.2$) and the fractional derivative order β_2 ($\alpha_2 = 0.8$) for fixed $\tau_q = 0.1$, $\tau_T = 0.1$, $Nr = 0.75$, $Pr = 6.8$, and $Q = 0.5$.

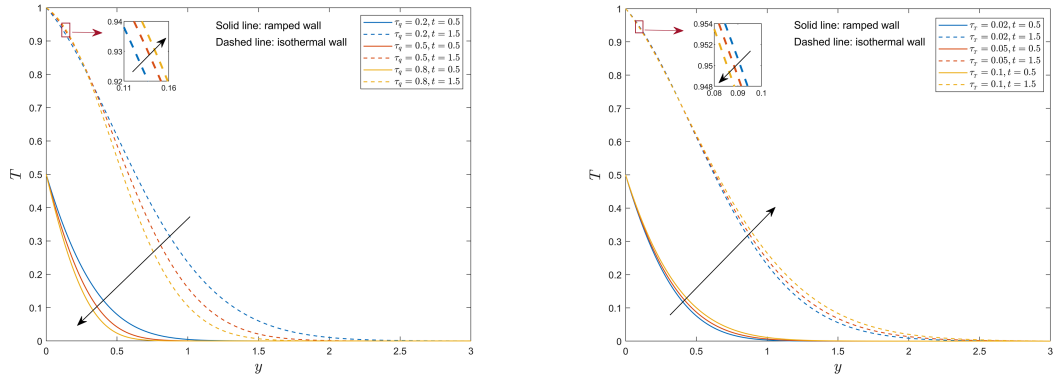

(a) Effects of τ_q **(b)** Effects of τ_T

Figure 8. Temperature distribution for the time lag of the heat flux τ_q ($\tau_T = 0.1$) and the temperature gradient τ_T ($\tau_q = 0.1$) for fixed $\alpha_2 = 0.8$, $\beta_2 = 0.7$, $Nr = 0.75$, $Pr = 6.8$, and $Q = 0.5$.

5.3. Effects on both velocity and temperature distributions

The effect of nanoparticle volume fraction φ on velocity and temperature distributions is illustrated in Figure 9. Under both ramped and isothermal wall temperature conditions, the nanofluid velocity exhibits an inverse relationship with φ (see Figure 9(a)). This can be attributed to the increase in the effective viscosity with φ, which enhances the flow resistance and suppresses the fluid motion. In contrast, the thermal boundary layer thickness increases with φ, indicating a reduction in heat transfer efficiency (see Figure 9(b)). Physically, the addition of nanoparticles enhances the effective thermal conductivity of the nanofluid, which promotes thermal diffusion and leads to a thicker thermal boundary layer. Figure 10 depicts the temporal evolution of velocity and temperature distributions.

Under both ramped and isothermal wall temperature conditions, the boundary layer thickness increases over time t, reflecting the system's transient response to thermal and momentum diffusion. Figure 11 presents the influence of heat source parameter Q on velocity and temperature distributions, where $Q > 0$ indicates heat injection and $Q < 0$ represents heat suction. The results demonstrate that both velocity and temperature distributions increase with increasing Q. Physically, heat injection raises the kinetic energy of nanofluid molecules and improves the internal energy of the nanofluid, resulting in enhancement of velocity and temperature. Figure 12 shows the effects of the thermal radiation parameter Nr on velocity and temperature distributions. Similar to Q, increasing Nr promotes the development of the velocity and temperature boundary layers.

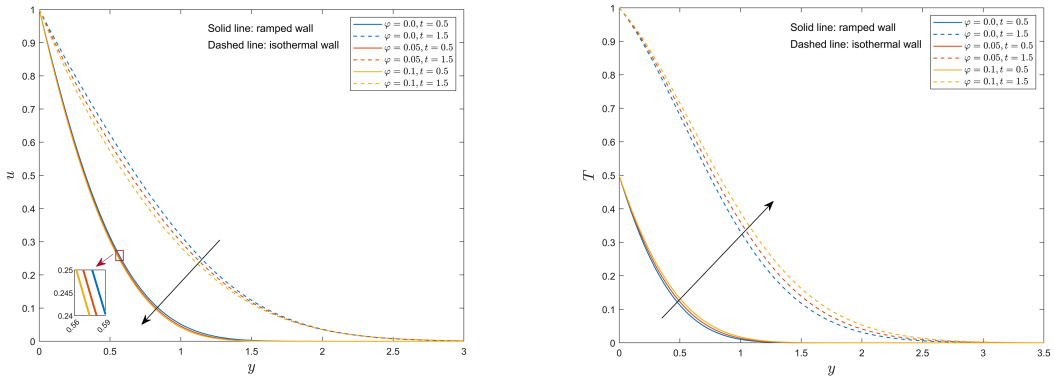

(a) Effects of φ on u **(b)** Effects of φ on T

Figure 9. Velocity and temperature distributions for the nanoparticle volume fraction φ of the Cu-water nanofluid, where (a) $\lambda = 0.1$, $\alpha_1 = 0.2$, $\beta_1 = 0.5$, $B = 2$, $K = 0.1$, and $Gr = 7$; (b) $\alpha_2 = 0.8$, $\beta_2 = 0.2$, $\tau_q = \tau_T = 0.1$, $Nr = 0.75$, $Pr = 6.8$, and $Q = 0.5$.

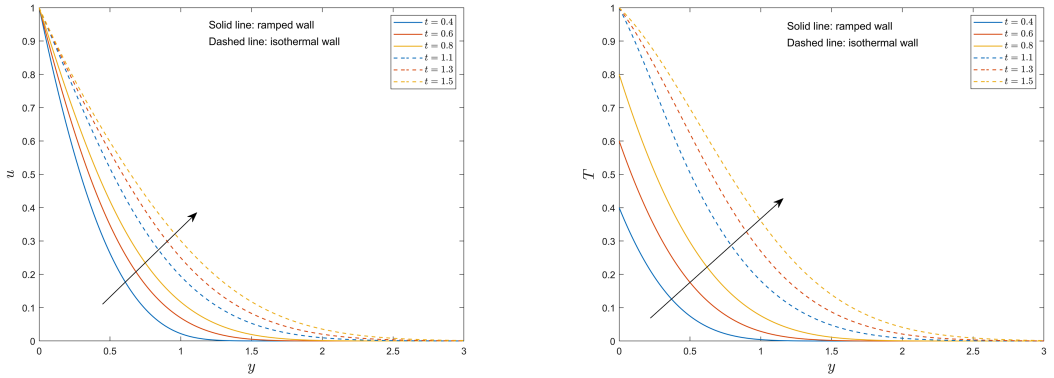

(a) Effects of t on u **(b)** Effects of t on T

Figure 10. Velocity and temperature distributions for time t, where (a) $\lambda = 0.1$, $\alpha_1 = 0.2$, $\beta_1 = 0.5$, $B = 2$, $K = 0.1$, and $Gr = 7$; (b) $\alpha_2 = 0.8$, $\beta_2 = 0.2$, $\tau_q = \tau_T = 0.1$, $Nr = 0.75$, $Pr = 6.8$, and $Q = 0.5$.

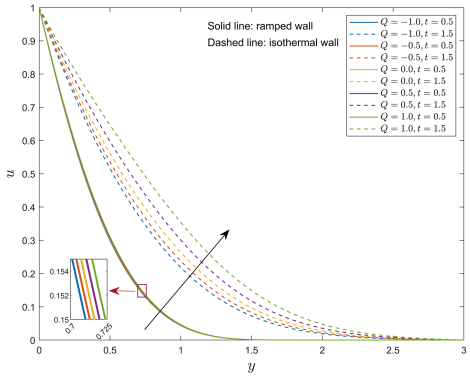

(a) Effects of Q on u

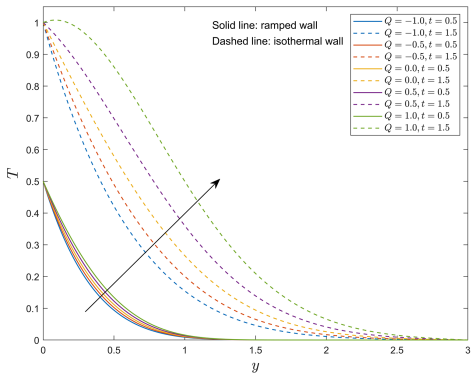

(b) Effects of Q on T

Figure 11. Velocity and temperature distributions for the heat injection/consumption constant Q, where (a) $\lambda = 0.1$, $\alpha_1 = 0.2$, $\beta_1 = 0.5$, $B = 2$, $K = 0.1$, and $Gr = 7$; (b) $\alpha_2 = 0.8$, $\beta_2 = 0.2$, $\tau_q = \tau_T = 0.1$, $Nr = 0.75$, and $Pr = 6.8$.

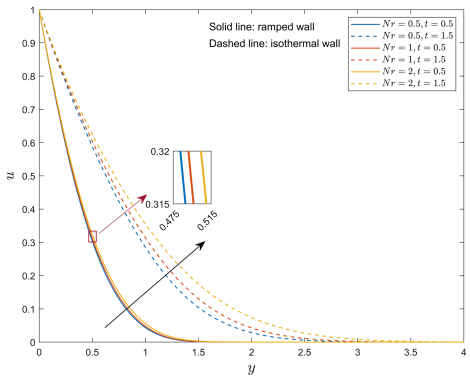

(a) Effects of Nr on u

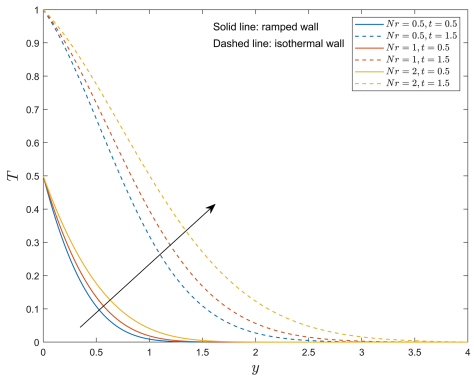

(b) Effects of Nr on T

Figure 12. Velocity and temperature distributions for the radiation parameter Nr, where (a) $\lambda = 0.1$, $\alpha_1 = 0.2$, $\beta_1 = 0.5$, $B = 2$, $K = 0.1$, and $Gr = 7$; (b) $\alpha_2 = 0.8$, $\beta_2 = 0.2$, $\tau_q = \tau_T = 0.1$, $Q = 0.5$, and $Pr = 6.8$.

As depicted in Figure 13, the velocity and temperature boundary layer thicknesses significantly decrease as the Prandtl number Pr rises. This effect is more pronounced under isothermal wall temperature conditions compared to ramped wall temperature conditions. Figure 14(a) presents the velocity profiles for three distinct nanofluids (Cu-water, Ag-water, and TiO_2-water) at a fixed $\varphi = 0.05$. The velocity profiles exhibit nonmonotonic behavior, with the Ag-water nanofluid displaying the lowest velocity after a certain intersection point. This behavior occurs because Ag has the largest density among the studied nanoparticles, increasing the inertia of nanofluid and reducing flow velocity. Additionally, the velocities of Cu-water and Ag-water nanofluids are relatively similar, likely due to their small density difference. Figure 14(b) illustrates the temperature distribution for different nanofluids. The thermal boundary layer is the thickest in the Ag-water nanofluid and the

thinnest in the TiO_2-water nanofluid. This trend is mainly attributed to the thermal conductivity of the nanoparticles: Ag possesses the highest thermal conductivity among the three, whereas TiO_2 displays the lowest, which reflects the influence of nanoparticle-fluid interactions on heat transport.

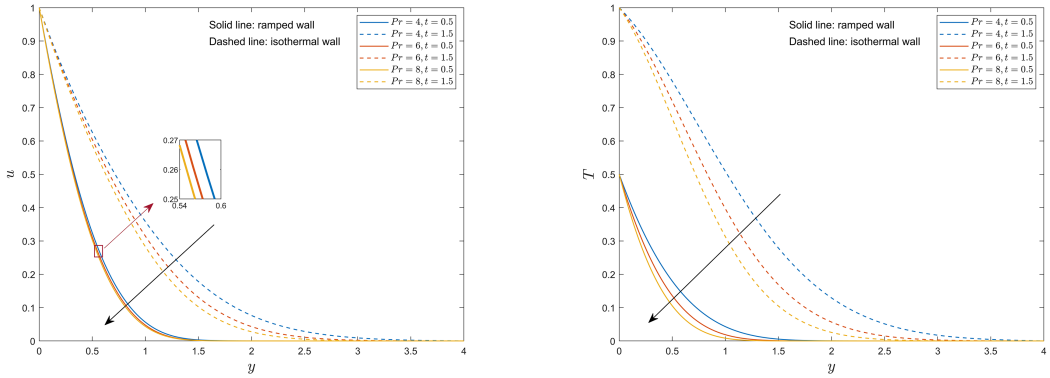

(a) Effects of Pr on u **(b)** Effects of Pr on T

Figure 13. Velocity and temperature distributions for the Prandtl number Pr, where (a) $\lambda = 0.1$, $\alpha_1 = 0.2$, $\beta_1 = 0.5$, $B = 2$, $K = 0.1$, and $Gr = 7$; (b) $\alpha_2 = 0.8$, $\beta_2 = 0.2$, $\tau_q = \tau_T = 0.1$, $Q = 0.5$, and $Nr = 0.75$.

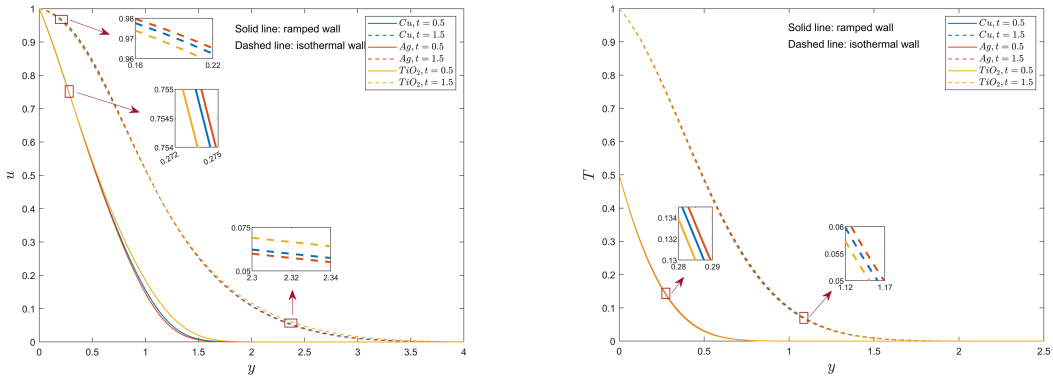

(a) Effects of different nanofluids on u **(b)** Effects of different nanofluids on T

Figure 14. Velocity and temperature distributions for the different nanofluids, where (a) $\lambda = 0.1$, $\alpha_1 = 0.2$, $\beta_1 = 0.5$, $B = 0.2$, $K = 0.3$, and $Gr = 6.5$; (b) $\alpha_2 = 0.8$, $\beta_2 = 0.8$, $\tau_q = 0.1$, $\tau_T = 0.01$, $Q = 0.5$, $Nr = 0.01$, and $Pr = 6.8$.

5.4. Application-oriented interpretation of the parametric results

To further connect the above parametric analyses from an application-oriented perspective, we briefly discuss their implications for regulating nanofluid flow and heat transfer under different operating conditions. The numerical results indicate that several parameters can be adjusted to control the transport behavior of the system. For example, increasing the relaxation parameter λ or the

fractional integral order β_1 tends to suppress the velocity boundary layer, which may be beneficial for stabilizing the flow in porous or thermally sensitive environments. In contrast, a larger fractional derivative order α_1 enhances the fluid response due to stronger memory effects. In the thermal field, the phase-lag parameters τ_q and τ_T play an important role in determining the development of the thermal boundary layer and the propagation speed of heat. Therefore, by appropriately tuning these parameters under different heating conditions, such as ramped wall temperature or isothermal heating, the flow intensity and heat transfer characteristics of viscoelastic nanofluids can be effectively regulated. This observation provides useful guidance for the design and control of nanofluid-based thermal management systems.

The present modeling framework may also have potential relevance in several modern thermal engineering applications involving complex fluids. For instance, viscoelastic nanofluids have been widely investigated for use in microchannel heat sinks, advanced cooling systems, and energy transport devices due to their enhanced heat transfer capability. In such systems, memory effects and non-Fourier heat conduction may become important when the characteristic time scales of heat transport are comparable to the relaxation time of the fluid. The ramped wall temperature condition considered in this work can represent gradual heating processes that commonly occur during the start-up stage of thermal devices or controlled heating operations. Therefore, the present fractional viscoelastic nanofluid model and the associated numerical results may provide useful insight into regulating flow structures and optimizing heat transfer performance in practical thermal management applications.

6. Conclusions

In this paper, the unsteady MHD flow and heat transfer of fractional viscoelastic nanofluids over an infinite vertical plate embedded in a porous medium were investigated under ramped and isothermal wall temperature conditions, together with heat injection/consumption effects. A fractional integrodifferential model was established by employing a dual-parameter fractional Maxwell constitutive relation for the momentum equation and a fractional dual-phase-lag model for the energy equation. The resulting coupled governing equations were then solved numerically by a finite difference framework based on the L1 algorithm and the weighted-shifted Grünwald difference scheme. The accuracy of the proposed numerical scheme was verified through manufactured solutions, and its reliability was further supported by comparisons with several classical nanofluid models. Finally, the effects of the key physical parameters on the velocity and temperature distributions were systematically examined. The key conclusions of this study are summarized as follows:

(i) The velocity and temperature distributions respond similarly to most parameters under both ramped and isothermal wall conditions. However, the time lags of the heat flux τ_q and the temperature gradient τ_T affect the temperature profile differently: the variation is monotonic under ramped wall temperature conditions but nonmonotonic under isothermal wall temperature conditions. This indicates that the wall heating mode plays an essential role in the transient development of the thermal boundary layer.

(ii) The fractional parameters have pronounced effects on both the flow and thermal fields. The velocity boundary layer thickness decreases with increasing relaxation parameter λ and fractional

integral index β_1, whereas the fractional derivative order α_1 has the opposite effect and leads to a thicker velocity boundary layer. In addition, the fractional parameters α_2 and β_2 exhibit opposite influences on the thermal boundary layer development. These results demonstrate that different fractional parameters play distinct roles in characterizing the memory-dependent momentum and heat transfer behavior of the nanofluid.

(iii) An increase in the nanoparticle volume fraction φ enhances the temperature distribution but suppresses the velocity distribution. The effects of different nanofluid types, including Cu-water, Ag-water, and TiO_2-water, on the velocity field are nonmonotonic. In particular, the Ag-water nanofluid exhibits the lowest velocity beyond a certain intersection point, mainly due to the relatively higher density of Ag nanoparticles.

(iv) The classical physical parameters also play important roles in the transient transport process. The magnetic parameter B suppresses the flow and reduces the velocity boundary layer thickness, whereas the permeability parameter K promotes the flow development. Furthermore, both the velocity and temperature distributions increase with increasing Grashof number Gr, radiation parameter Nr, and heat injection/consumption constant Q. In terms of parameter sensitivity, the velocity field is particularly responsive to β_1 and K, while the thermal field shows stronger sensitivity to τ_T.

In this study, the governing boundary-layer equations were solved using the finite difference method to investigate the MHD flow and heat transfer of nanofluids under ramped and isothermal wall temperature conditions. The numerical results demonstrate that the proposed fractional model provides an effective framework for describing the memory-dependent flow and thermal transport behavior in porous thermal systems. Future work may focus on improving the computational efficiency by employing adaptive algorithms in the temporal direction [56, 57]. In addition, fast algorithms for fractional operators, such as the sum-of-exponentials approximation [58] and parallel-in-time methods [59], could be considered to reduce the computational cost caused by the history dependence of fractional derivatives. Furthermore, the present framework may be extended to incorporate nanoparticle slip mechanisms, including Brownian diffusion and thermophoretic effects [60].

Nomenclature

B	Magnetic parameter	(–)
B_0	Imposed magnetic field	(T)
C_p	Isobaric heat capacity	$(J{\cdot}kg^{-1}{\cdot}K^{-1})$
${}^{C}D_t^{\alpha}$	Caputo fractional derivative	(–)
${}^{RL}D_t^{\alpha}$	Riemann–Liouville fractional derivative	(–)
E	Shear modulus	(Pa)
g	Gravitational acceleration	$(m{\cdot}s^{-2})$
Gr	Grashof number	(–)
h	Heat transfer coefficient	$(W{\cdot}m^{-2}{\cdot}K^{-1})$
I_t^{α}	Riemann–Liouville fractional integral	(–)
k	Thermal conductivity	$(W{\cdot}m^{-1}{\cdot}K^{-1})$
k_R	Rosseland mean absorption coefficient	(m^{-1})
K	Permeability parameter	(–)
K'	Permeability of medium	(m^2)
L	Characteristic length	(m)
N_r	Thermal radiation parameter	(–)
Pr	Prandtl number	(–)
q	Heat flux	$(W{\cdot}m^{-2})$
q_r	Radiative heat flux	$(W{\cdot}m^{-2})$
Q	Heat injection/consumption parameter	(–)

Greek symbols

α	Fractional order	(–)
α_1	Fractional order	(–)
α_2	Fractional order	(–)
β_1	Fractional order	(–)
β_2	Fractional order	(–)
β_T	Volumetric thermal expansion coefficient	(K^{-1})
γ	Fractional order	(–)
ε	Shear strain	(–)
λ	Velocity relaxation time	(s)
μ	Dynamic viscosity	(Pa·s)
ν	Kinematic viscosity ($\nu = \mu/\rho$)	$(m^2{\cdot}s^{-1})$
ρ	Density	$(kg{\cdot}m^{-3})$
σ	Shear stress	(Pa)
σ_e	Electrical conductivity	$(S{\cdot}m^{-1})$
σ_{xy}	Shear stress	(Pa)
σ_{SB}	Stefan–Boltzmann constant	$(W{\cdot}m^{-2}{\cdot}K^{-4})$
σ'	Ratio of electrical conductivity	(–)
τ	Dimensionless constant	(–)
τ_q	Time lag of heat flux	(s)
τ_T	Time lag of temperature gradient	(s)

Nomenclature

Q_0	Heat injection/consumption constant	($W \cdot m^{-3}$)
t_0	Specified time ($t_0 = \nu_{nf}/u_0^2$)	(s)
T	Nanofluid temperature	(K)
T_∞	Ambient temperature	(K)
u	Nanofluid velocity	($m \cdot s^{-1}$)
u_0	Plate velocity	($m \cdot s^{-1}$)

Greek symbols

φ	Nanoparticle volume fraction	(–)

Subscripts

eff	Effective
bf	Base fluid
nf	Nanofluid
np	Nanoparticle
w	Wall condition

Use of AI tools declaration

The authors declare they have not used Artificial Intelligence (AI) tools in the creation of this article.

Acknowledgments

This research was supported by the National Natural Science Foundation of China (Grant No. 12471391), the Science and Technology Foundation of Guizhou Province of China (Grant No. MS (2026) 798), the Australian Research Council via the Discovery Project DP230102414, the Research and Development Project of Henan Province (Science and Technology Cooperation Project, No. 252102521012), and the Scientific Research Project of Jishou University (No. Jdy24037).

Conflict of interest

The authors declare there is no conflict of interest.

Author contributions

Huafang Li: Conceptualization, Methodology, Software, Validation, Writing – original draft. **Zhi Mao:** Investigation, Software, Validation, Writing – original draft, Funding acquisition. **Aiguo Xiao:** Methodology, Validation, Funding acquisition. **Libo Feng:** Writing – review and editing, Supervision, Funding acquisition. **Leilei Wei:** Methodology, Writing – review and editing, Funding acquisition. **Fawang Liu:** Supervision, Writing – review and editing.

References

1. S. U. S. Choi, J. A. Eastman, Enhancing thermal conductivity of fluids with nanoparticles, in *ASME's International Mechanical Engineering Congress & Exposition*, ASME, **66** (1995), 99–105. https://doi.org/10.1115/IMECE1995-0926
2. W. Yu, D. M. France, J. L. Routbort, S. U. S. Choi, Review and comparison of nanofluid thermal conductivity and heat transfer enhancements, *Heat Transfer Eng.*, **29** (2008), 432–460. https://doi.org/10.1080/01457630701850851
3. M. U. Sajid, H. M. Ali, Thermal conductivity of hybrid nanofluids: A critical review, *Int. J. Heat Mass Transfer*, **126** (2018), 211–234. https://doi.org/10.1016/j.ijheatmasstransfer.2018.05.021

4. J. A. Eastman, S. U. S. Choi, S. Li, W. Yu, L. J. Thompson, Anomalously increased effective thermal conductivities of ethylene glycol-based nanofluids containing copper nanoparticles, *Appl. Phys. Lett.*, **78** (2001), 718–720. https://doi.org/10.1063/1.1341218

5. O. Mahian, L. Kolsi, M. Amani, P. Estellé, G. Ahmadi, C. Kleinstreuer, et al., Recent advances in modeling and simulation of nanofluid flows—Part I: Fundamentals and theory, *Phys. Rep.*, **790** (2019), 1–48. https://doi.org/10.1016/j.physrep.2018.11.004

6. D. D. Kumar, A. V. Arasu, A comprehensive review of preparation, characterization, properties and stability of hybrid nanofluids, *Renewable Sustainable Energy Rev.*, **81** (2018), 1669–1689. https://doi.org/10.1016/j.rser.2017.05.257

7. P. C. Mishra, S. Mukherjee, S. K. Nayak, A. Panda, A brief review on viscosity of nanofluids, *Int. Nano Lett.*, **4** (2014), 109–120. https://doi.org/10.1007/s40089-014-0126-3

8. J. Zhao, L. Zheng, X. Zhang, F. Liu, Unsteady natural convection boundary layer heat transfer of fractional Maxwell viscoelastic fluid over a vertical plate, *Int. J. Heat Mass Transfer*, **97** (2016), 760–766. https://doi.org/10.1016/j.ijheatmasstransfer.2016.02.059

9. M. Shen, L. Chen, M. Zhang, F. Liu, A renovated Buongiorno's model for unsteady Sisko nanofluid with fractional Cattaneo heat flux, *Int. J. Heat Mass Transfer*, **126** (2018), 277–286. https://doi.org/10.1016/j.ijheatmasstransfer.2018.05.131

10. L. Liu, L. Feng, Q. Xu, L. Zheng, F. Liu, Flow and heat transfer of generalized Maxwell fluid over a moving plate with distributed order time fractional constitutive models, *Int. Commun. Heat Mass Transfer*, **116** (2020), 104679. https://doi.org/10.1016/j.icheatmasstransfer.2020.104679

11. L. Feng, F. Liu, I. Turner, V. V. Anh, Magnetohydrodynamics flow and heat transfer of novel generalized Kelvin–Voigt viscoelastic nanofluids over a moving plate, *Phys. Fluids*, **36** (2024), 063109. https://doi.org/10.1063/5.0213855

12. Z. Mao, L. Feng, I. Turner, A. Xiao, F. Liu, Transient free convective flow of viscoelastic nanofluids governed by fractional integrodifferential equations under Newtonian heating and thermal radiation, *Chin. J. Phys.*, **93** (2025), 584–600. https://doi.org/10.1016/j.cjph.2024.12.025

13. M. Omama, A. A. Arafa, A. Elsaid, W. K. Zahra, Numerical analysis of double-fractional PDEs in MHD hybrid nanofluid blood flow with slip velocity, heat source, and radiation effects, *Phys. Scr.*, **100** (2024), 015288. https://doi.org/10.1088/1402-4896/ada06f

14. H. Sun, Y. Jiang, Y. Zhang, L. Jiang, A review of constitutive models for non-Newtonian fluids, *Fract. Calc. Appl. Anal.*, **27** (2024), 1483–1526. https://doi.org/10.1007/s13540-024-00294-0

15. L. Feng, I. Turner, V. V. Anh, F. Liu, Review of classical and nonlocal nanofluid models for solar collectors, *Renewable Sustainable Energy Rev.*, **212** (2025), 115382. https://doi.org/10.1016/j.rser.2025.115382

16. E. R. Priest, T. G. Forbes, The magnetic nature of solar flares, *Astron. Astrophys. Rev.*, **10** (2002), 313–377. https://doi.org/10.1007/s001590100013

17. K. Rafique, Z. Mahmood, U. Khan, Mathematical analysis of MHD hybrid nanofluid flow with variable viscosity and slip conditions over a stretching surface, *Mater. Today Commun.*, **36** (2023), 106692. https://doi.org/10.1016/j.mtcomm.2023.106692

18. A. J. Chamkha, A. M. Aly, MHD free convection flow of a nanofluid past a vertical plate in the presence of heat generation or absorption effects, *Chem. Eng. Commun.*, **198** (2010), 425–441. https://doi.org/10.1080/00986445.2010.520232

19. T. Anwar, P. Kumam, D. Baleanu, I. Khan, P. Thounthong, Radiative heat transfer enhancement in MHD porous channel flow of an Oldroyd-B fluid under generalized boundary conditions, *Phys. Scr.*, **95** (2020), 115211. https://doi.org/10.1088/1402-4896/abbe50

20. G. Dharmaiah, O. D. Makinde, K. S. Balamurugan, Influence of magneto hydro dynamics (MHD) nonlinear radiation on micropolar nanofluid flow over a stretching surface: Revised Buongiorno's nanofluid model, *J. Nanofluids*, **11** (2022), 1009–1022. https://doi.org/10.1166/jon.2022.1890

21. S. G. Bejawada, M. M. Nandeppanavar, Effect of thermal radiation on magnetohydrodynamics heat transfer micropolar fluid flow over a vertical moving porous plate, *Exp. Comput. Multiphase Flow*, **5** (2023), 149–158. https://doi.org/10.1007/s42757-021-0131-5

22. S. Saleem, T. Abbas, H. Abutuqayqah, E. U. Haq, S. U. Khan, Numerical simulation accompanied by an intelligent computing system for the chemical reaction of Casson nanofluid and radiative heat flux on a nonlinear stretching surface, *Alexandria Eng. J.*, **79** (2023), 629–643. https://doi.org/10.1016/j.aej.2023.08.016

23. Z. Sheng, Y. Liu, Y. Li, Unsteady magnetohydrodynamic flow, heat, and mass transfer of the fractional Oldroyd-B fluid along a moving infinite vertical plate, *Phys. Fluids*, **37** (2025), 113114. https://doi.org/10.1063/5.0293008

24. S. Kavya, V. Nagendramma, N. A. Ahammad, S. Ahmad, C. S. K. Raju, N. A. Shah, Magnetic-hybrid nanoparticles with stretching/shrinking cylinder in a suspension of MoS4 and copper nanoparticles, *Int. Commun. Heat Mass Transfer*, **136** (2022), 106150. https://doi.org/10.1016/j.icheatmasstransfer.2022.106150

25. P. Jalili, A. A. Azar, B. Jalili, D. D. Ganji, Study of nonlinear radiative heat transfer with magnetic field for non-Newtonian Casson fluid flow in a porous medium, *Results Phys.*, **48** (2023), 106371. https://doi.org/10.1016/j.rinp.2023.106371

26. C. P. Malhotra, R. L. Mahajan, W. S. Sampath, K. L. Barth, R. A. Enzenroth, Control of temperature uniformity during the manufacture of stable thin-film photovoltaic devices, In *ASME International Mechanical Engineering Congress and Exposition*, **4711** (2004), 547–555. https://doi.org/10.1115/IMECE2004-61331

27. N. Ahmed, M. Dutta, Transient mass transfer flow past an impulsively started infinite vertical plate with ramped plate velocity and ramped temperature, *Int. J. Phys. Sci.*, **8** (2013), 254–263. https://doi.org/10.5897/IJPS12.713

28. P. Chandran, N. C. Sacheti, A. K. Singh, Natural convection near a vertical plate with ramped wall temperature, *Heat Mass Transfer*, **41** (2005), 459–464. https://doi.org/10.1007/s00231-004-0568-7

29. G. S. Seth, M. S. Ansari, R. Nandkeolyar, MHD natural convection flow with radiative heat transfer past an impulsively moving plate with ramped wall temperature, *Heat Mass Transfer*, **47** (2011), 551–561. https://doi.org/10.1007/s00231-010-0740-1

30. S. Rao, P. N. Deka, Numerical analysis of MHD hybrid nanofluid flow a porous stretching sheet with thermal radiation, *Int. J. Appl. Comput. Math.*, **10** (2024), 95. https://doi.org/10.1007/s40819-024-01734-4

31. M. VeeraKrishna, A. J. Chamkha, Hall effects on unsteady MHD flow of second grade fluid through porous medium with ramped wall temperature and ramped surface concentration, *Phys. Fluids*, **30** (2018), 053101. https://doi.org/10.1063/1.5025542

32. Y. D. Reddy, B. S. Goud, M. A. Kumar, Radiation and heat absorption effects on an unsteady MHD boundary layer flow along an accelerated infinite vertical plate with ramped plate temperature in the existence of slip condition, *Partial Differ. Equ. Appl. Math.*, **4** (2021), 100166. https://doi.org/10.1016/j.padiff.2021.100166

33. Z. Mao, L. Feng, A. Xiao, F. Liu, I. Turner, Magnetohydrodynamic transient flow of dual-parameter fractional Maxwell nanofluids past a vertical plate with generalised dual-phase-lagging heat conduction under ramped wall temperature conditions, *Eng. Comput.*, **42** (2026), 51. https://doi.org/10.1007/s00366-025-02267-0

34. B. Jin, *Fractional Differential Equations*, Springer International Publishing, 2021. https://doi.org/10.1007/978-3-030-76043-4

35. F. Mainardi, G. Spada, Creep, relaxation and viscosity properties for basic fractional models in rheology, *Eur. Phys. J. Spec. Top.*, **193** (2011), 133–160. https://doi.org/10.1140/epjst/e2011-01387-1

36. *Applications of Fractional Calculus in Physics*, (ed. R. Hilfer), World Scientific, 2000. https://doi.org/10.1142/3779

37. H. Schiessel, R. Metzler, A. Blumen, T. F. Nonnenmacher, Generalized viscoelastic models: Their fractional equations with solutions, *J. Phys. A: Math. Gen.*, **28** (1995), 6567–6584. https://doi.org/10.1088/0305-4470/28/23/012

38. C. Friedrich, Relaxation and retardation functions of the Maxwell model with fractional derivatives, *Rheol. Acta*, **30** (1991), 151–158. https://doi.org/10.1007/BF01134604

39. W. Tan, W. Pan, M. Xu, A note on unsteady flows of a viscoelastic fluid with the fractional Maxwell model between two parallel plates, *Int. J. Non-Linear Mech.*, **38** (2003), 645–650. https://doi.org/10.1016/S0020-7462(01)00121-4

40. S. Rosseland, *Astrophysics: On an Atomic-Theoretical Basis*, Springer-Verlag, Berlin, 1931.

41. E. Magyari, A. Pantokratoras, Note on the effect of thermal radiation in the linearized Rosseland approximation on the heat transfer characteristics of various boundary layer flows, *Int. Commun. Heat Mass Transfer*, **38** (2011), 554–556. https://doi.org/10.1016/j.icheatmasstransfer.2011.03.006

42. D. Y. Tzou, The generalized lagging response in small-scale and high-rate heating, *Int. J. Heat Mass Transfer*, **38** (1995), 3231–3240. https://doi.org/10.1016/0017-9310(95)00052-B

43. T. N. Mishra, K. N. Rai, Numerical solution of FSPL heat conduction equation for analysis of thermal propagation, *Appl. Math. Comput.*, **273** (2016), 1006–1017. https://doi.org/10.1016/j.amc.2015.10.082

44. Z. M. Odibat, N. T. Shawagfeh, Generalized Taylor's formula, *Appl. Math. Comput.*, **186** (2007), 286–293. https://doi.org/10.1016/j.amc.2006.07.102

45. C. Ji, W. Dai, Z. Sun, Numerical method for solving the time-fractional dual-phase-lagging heat conduction equation with the temperature-jump boundary condition, *J. Sci. Comput.*, **75** (2018), 1307–1336. https://doi.org/10.1007/s10915-017-0588-3

46. H. Xu, X. Jiang, Time fractional dual-phase-lag heat conduction equation, *Chin. Phys. B*, **24** (2015), 034401. https://doi.org/10.1088/1674-1056/24/3/034401

47. Y. D. Reddy, B. S. Goud, Comprehensive analysis of thermal radiation impact on an unsteady MHD nanofluid flow across an infinite vertical flat plate with ramped temperature with heat consumption, *Results Eng.*, **17** (2023), 100796. https://doi.org/10.1016/j.rineng.2022.100796

48. M. Chandrasekar, S. Suresh, R. Srinivasan, A. C. Bose, New analytical models to investigate thermal conductivity of nanofluids, *J. Nanosci. Nanotechnol.*, **9** (2009), 533–538. https://doi.org/10.1166/jnn.2009.j025

49. L. Godson, B. Raja, D. M. Lal, S. Wongwises, Experimental investigation on the thermal conductivity and viscosity of silver–deionized water nanofluid, *Exp. Heat Transfer*, **23** (2010), 317–332. https://doi.org/10.1080/08916150903564796

50. E. Abu-Nada, Application of nanofluids for heat transfer enhancement of separated flows encountered in a backward facing step, *Int. J. Heat Fluid Flow*, **29** (2008), 242–249. https://doi.org/10.1016/j.ijheatfluidflow.2007.07.001

51. H. Schlichting, K. Gersten, *Boundary-Layer Theory*, Springer, Berlin, 2016. https://doi.org/10.1007/978-3-662-52919-5

52. S. Das, A. Sensharma, R. N. Jana, R. P. Sharma, Slip flow of nanofluid past a vertical plate with ramped wall temperature considering thermal radiation, *J. Nanofluids*, **6** (2017), 1054–1064. https://doi.org/10.1166/jon.2017.1392

53. B. Jin, Z. Zhou, *Numerical Treatment and Analysis of Time-Fractional Evolution Equations*, Springer Cham, 2023. https://doi.org/10.1007/978-3-031-21050-1

54. Z. Wang, S. Vong, Compact difference schemes for the modified anomalous fractional sub-diffusion equation and the fractional diffusion-wave equation, *J. Comput. Phys.*, **277** (2014), 1–15. https://doi.org/10.1016/j.jcp.2014.08.012

55. M. Khan, A. Rasheed, M.S. Anwar, S. T. Hussain Shah, Application of fractional derivatives in a Darcy medium natural convection flow of MHD nanofluid, *Ain Shams Eng. J.*, **14** (2023), 102093. https://doi.org/10.1016/j.asej.2022.102093

56. L. Liu, Y. Liang, X. Bao, H. Fang, An efficient adaptive grid method for a system of singularly perturbed convection-diffusion problems with Robin boundary conditions, *Adv. Differ. Equ.*, **2021** (2021), 6. https://doi.org/10.1186/s13662-020-03166-y

57. Z. Mao, D. Luo, A robust adaptive grid method for first-order nonlinear singularly perturbed Fredholm integro-differential equations, *Networks Heterogen. Media*, **18** (2023), 1006–1023. https://doi.org/10.3934/nhm.2023044

58. S. Jiang, J. Zhang, Q. Zhang, Z. Zhang, Fast evaluation of the Caputo fractional derivative and its applications to fractional diffusion equations, *Commun. Comput. Phys.*, **21** (2015), 650–678. https://doi.org/10.4208/cicp.OA-2016-0136

59. X. Gu, S. Wu, A parallel-in-time iterative algorithm for Volterra partial integro-differential problems with weakly singular kernel, *J. Comput. Phys.*, **417** (2020), 109576. https://doi.org/10.1016/j.jcp.2020.109576

60. J. Buongiorno, Convective transport in nanofluids, *J. Heat Transfer*, **128** (2006), 240–250. https://doi.org/10.1115/1.2150834

AIMS Press